

Identifying Split Vacancies with Foundation Models and Electrostatics

Seán R. Kavanagh*

Harvard University Center for the Environment, Cambridge, Massachusetts 02138,
United States

E-mail: skavanagh@seas.harvard.edu

Abstract. Point defects are ubiquitous in solid-state compounds, dictating many functional properties such as conductivity, catalytic activity and carrier recombination. Over the past decade, the prevalence of metastable defect geometries and their importance to relevant properties has been increasingly recognised. A particularly striking example of this is split vacancies, where an isolated atomic vacancy transforms to a stoichiometry-conserving complex of two vacancies and an interstitial ($V_X \rightarrow [V_X + X_i + V_X]$), which can be accompanied by a dramatic lowering of the defect energy and change in behaviour. Such species are particularly challenging to identify from computation, due to the ‘non-local’ nature of this reconstruction. Here, I present an approach for efficiently identifying such species in solid-state compounds, through tiered screening which combines geometric analysis, electrostatic energies and foundation machine learning (ML) models. This approach allows the screening of all compounds in the Materials Project database (including all entries in the ICSD, along with several thousand predicted metastable materials), identifying thousands of split vacancy configurations, hitherto unknown. This study highlights both the potential utility of machine-learning potentials for defect investigations, with important caveats, and the importance of global optimisation approaches for correctly identifying stable defect geometries.

Introduction

Point defects are an unavoidable feature of bulk solid-state materials, due to the large configurational entropy gain associated with their formation.^{1,2} These defects dictate functional properties and performance in many compounds and applications, from beneficial impacts in semiconductor doping, catalytic activity, ionic conductivity and single-photon emission, to detrimental effects on carrier recombination, pernicious absorption and chemical degradation, to name a handful.³ The characterisation and manipulation of defects in materials is thus a primary route to advancing a wide range of technological capabilities, particularly in the realm of energy materials such as solar photovoltaics, transparent conducting materials, batteries and (photo-)catalysts.⁴⁻⁸ In recent years, there has been renewed interest in the complexity of defect energy landscapes, with the potential for multiple different locally-stable configurations which contribute to the overall behaviour of the species.⁹⁻²⁰ This can arise when the defect can adopt multiple different bonding configurations, spin states or others. One of the first well-known examples of such metastability for defects was the case of the so-called ‘DX-centres’ in (Al)GaAs and Si, studied in the 1970s. Here, puzzling observations of transient behaviour,

persistent photoconductivity, charge compensation and large Stokes shifts led researchers to propose that donor defects (D) were forming complexes with an unknown acceptor defect (X) to compensate their charge.²¹ With the help of theoretical studies,²² it was later revealed that no other defect was involved in these processes, and rather the transformation was driven by the donor defect D displacing significantly off-site to a new bonding configuration, where a negative (acceptor) charge state was then stabilised. Crucially, there is a small energy barrier to this transition, and so a bias or thermal energy is required to observe this behaviour in either experiment or computation. Such metastability for point defects has since been shown to impact electron-hole recombination rates in LEDs and photovoltaic devices,^{10,16,23,24} oxidation and decomposition in battery cathodes,^{13,25} catalytic activity in oxides,²⁶ charge compensation in chalcogenides,²⁷ and absorption spectra in II-VI compounds,²⁸ to name a few.

A particularly striking case of such large defect reconstructions is that of ‘split vacancies’ where, starting from the simple vacancy picture, a nearby atom displaces toward an interstitial site adjacent to the vacancy, effectively creating an additional vacancy and interstitial in the process; Fig. 1a. A split vacancy can thus be thought of as a stoichiometry-conserving complex of two vacancies and an interstitial ($V_X \rightarrow X_i + 2V_X$). A dramatic lowering of the defect energy and change in behaviour can accompany this large structural transformation. For instance, one of the most well-known cases of split vacancies is that of V_{Ga} in Ga_2O_3 , which has been extensively studied as a promising material for power electronics and transparent conducting oxides.^{19,29} As reported by Varley *et al.*¹⁷ and shown in Fig. 1b, negatively-charged Ga vacancies — the dominant acceptor species — can form split-vacancy complexes which lower their energy by $\sim 1\text{eV}$.^[1] This transformation has several crucial implications for the electronic and defect behaviour of Ga_2O_3 . Firstly, the large energy lowering of the negatively-charged cation vacancy (V_{Ga}^{-3}) greatly increases its concentration and makes it a shallower acceptor species. Being the most favourable intrinsic acceptor in Ga_2O_3 — which is typically doped *n*-type — this places greater limitations on electron dopability by reducing the electron doping window and enhancing ionic charge compensation. Moreover, the split vacancy geometry of V_{Ga} is found to be key to ion migration pathways,³³ which are relevant for the diffusion of technologically-important dopants and impurities in Ga_2O_3 . These split configurations of Ga vacancies in Ga_2O_3 have since been verified by a number of experimental measurements, including positron annihilation spectroscopy,^{34,35} electron paramagnetic resonance (EPR),^{36,37} scanning transmission electron microscopy (STEM),³⁸ and vibrational spectroscopy with hydrogenated samples.^{39–41}

Such split vacancies have since been shown to exist in a small handful of other structurally-related and technologically-relevant compounds, such as the $R\bar{3}c$ corundum-structured polymorph α - Ga_2O_3 , along with corundum-like compounds; Al_2O_3 , In_2O_3 , Ca_3N_2 and Mg_3N_2 .^{12,14,30} Earlier this year, Fowler *et al.*¹⁴ discussed the known cases of these split vacancies; including those mentioned above, beta-tridymite SiO_2 and a handful of metastable split vacancies in some rutile compounds and Cu_2O . In an investigation of Sb_2O_5 as a candidate transparent conducting oxide earlier this year, Li *et al.*⁴⁷ reported a split-vacancy structure for V_{Sb} found using the **ShakeNBreak**^{9,42} approach, which lowers the vacancy energy by over 2 eV. While this small set of known split vacancy geometries is mostly comprised of *cation* vacancy defects, split vacancy structures have also been observed for some *anion* vacancies, such as V_{O} in TiO_2 ⁴⁵ & Ba_2TiO_4 ⁴⁶ and V_{N} in Mg_3N_2 & Ca_3N_2 ¹⁴.

Theoretical methods often represent the primary avenue for the investigation of point defects at the atomic scale, due to an inherent difficulty in experimentally characterising dilute localised species. Computational predictions of defect behaviour (and resultant impact) are often then compared to experimental measurements of downstream global properties, such as carrier concentrations, solar cell efficiency, ionic conductivity or catalytic activity. The accuracy of such computational approaches, when employing appropriate levels of theory and careful

[1] This behaviour was originally reported for monoclinic $C2/m$ β - Ga_2O_3 , but has since been observed for the corundum-structured $R\bar{3}c$ α and orthorhombic κ phases as well.^{14,30–32}

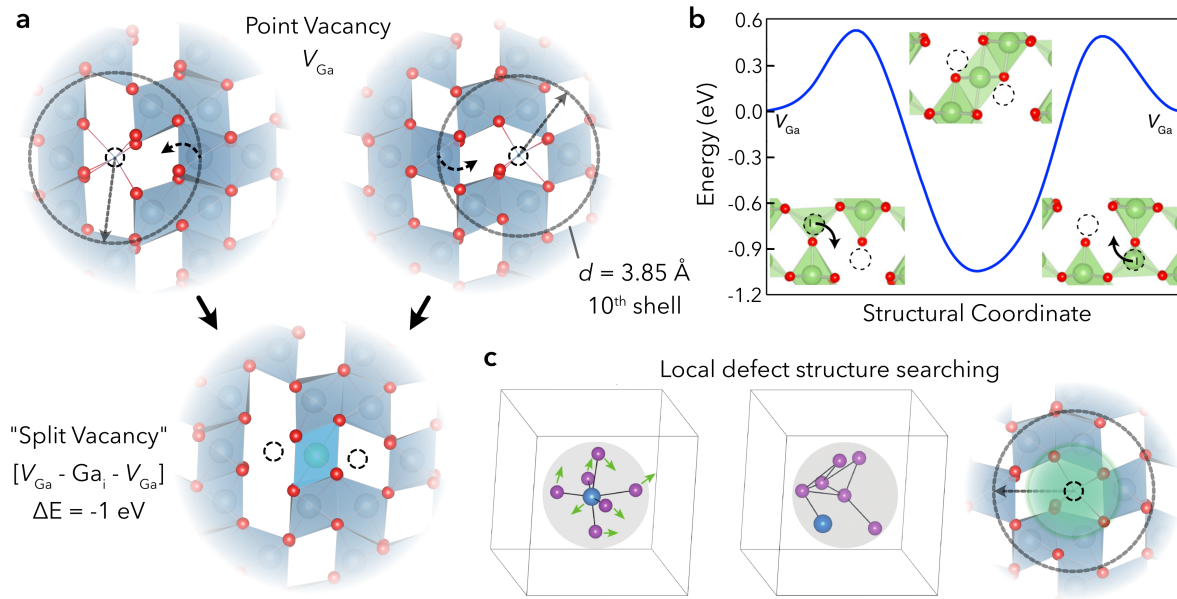


Figure 1. Split vacancy configurations in solids. **(a)** Schematic illustration of the transformation from a single atomic vacancy (top) to a split vacancy geometry (bottom) using V_{Ga} in $R\bar{3}c$ α - Ga_2O_3 as an example. Vacancy positions are indicated by the hollow circles, curved arrows depict the movement of the neighbouring cation in transforming from the single vacancy to the split vacancy, and dashed grey circles depict the 10th neighbour shell of the vacancy site ($d = 3.85 \text{ \AA}$). In the bottom image, the interstitial cation within the split vacancy ($[V_X + X_i + V_X]$) is highlighted in lighter blue. **(b)** Potential energy surface (PES) of the tetrahedral-site Ga vacancy in $C2/m$ β - Ga_2O_3 , along the symmetric path from the single vacancy (endpoints) to the split vacancy (middle), adapted with permission from Varley *et al.*¹⁷ **(c)** Structure searching methods employed for point defects, comprising targeted⁴² or random^{43–46} local bond distortions (left) and/or chemical identity permutations (centre). Adapted with permission from Huang *et al.*⁴³. Typical search radii for defect reconstructions are depicted by the shaded green area for V_{Ga} α - Ga_2O_3 on the right, significantly smaller than the $V_X - V_X$ distance in $[V_X + X_i + V_X]$ split-vacancy complexes.

methodology, has been well verified through comparisons with experiment.^{1,2,10,40} Metastability at defects presents a challenge to computational methods, however. Defect modelling involves the simulation of a defect embedded in the bulk compound (typically using a large periodic supercell), from which the formation energy and related properties can be computed. This requires some initialisation of the defect state in terms of geometry and spin, before relaxing to the local minimum energy arrangement – typically via gradient descent. However, when defects exhibit multiple locally-stable minima, this single predicted arrangement will not give the full picture of defect behaviour. In many cases, this state will be a higher-energy metastable configuration, which can lead to inaccurate predictions of defect properties, such as defect and charge-carrier concentrations, recombination activity, diffusion barriers and more. Indeed, as implied by the potential energy surface (PES) in Fig. 1b, the identification of the split vacancy V_{Ga} in β - Ga_2O_3 was a serendipitous discovery by Varley *et al.*,¹⁷ where a Nudged Elastic Band (NEB) calculation of the (simple) vacancy migration pathway revealed that the expected transition state (the split vacancy) was in fact the ground-state arrangement. A handful of approaches have been proposed to counteract this issue and target a global optimisation strategy for defects.^{9,11,42–45} In particular, the ShakeNBreak⁴² method has been used to demonstrate the prevalence and importance of such defect reconstructions across diverse materials classes.⁹ Within this approach, a set of candidate geometries are generated by distorting the local bonding environment of the defect according to some simple chemical guiding principles, along with constrained random displacements (‘rattling’) to break symme-

try and disrupt the long-range lattice potential, in order to coarsely sample various regions of the defect energy landscape. Despite its relative simplicity and computational efficiency, this approach has been found to perform surprisingly well in identifying structural reconstructions and metastabilities at defects.

Split vacancies present a distinct challenge to current defect structure-searching approaches however, with most failing to identify ground-states split vacancy geometries in the majority of cases. This can be attributed to the built-in locality of these optimisation approaches, which attempt to leverage our physical intuition regarding defect behaviour to bias the search space and boost computational efficiency. Namely, these approaches make use of the ‘molecule-in-a-solid’ nature of defects, where interactions are inherently short-range and dominated by the first and next-nearest neighbours, with most (known) defect reconstructions involving some perturbation of this highly-*local* bonding environment. As such, these approaches often start from the unperturbed defect structure (e.g. the simple removal of an atom to create a vacancy, or mutation of the chemical identity to create a substitution), and then apply *local* geometry perturbations to efficiently scan accessible reconstructions, as depicted in Fig. 1c. The transformation of isolated vacancies to split vacancies; $V_X \rightarrow X_1 + 2V_X$, is a *non-local* process however, as it involves the movement of a host atom which is initially quite far from the defect site (3.85 Å for V_{Ga} in $\alpha\text{-Ga}_2\text{O}_3$ – Fig. 1a, corresponding to the 10th nearest-neighbour shell or the 28th closest atom) to a position much closer to the original vacancy site — around the midpoint of the original separation. This point is further verified by structural analysis of split vacancies identified in this work, shown in Fig. S2, where the largest atomic displacements relative to bulk positions occur for atoms located 3-5 Å away from the single vacancy site for split vacancies, as opposed to 1-2 Å for simple point vacancies. Consequently, ‘local’ structure-searching methods such as **ShakeNBreak** which target distortions involving the first few neighbour shells are expected to struggle at identifying these ‘non-local’ reconstructions.

Indeed, both in this work and in unpublished work from Dr Joel Varley, it was confirmed that **ShakeNBreak** fails to identify the split-vacancy groundstate for V_{Ga} in Ga_2O_3 , when starting from the isolated vacancy geometry. On the other hand, **ShakeNBreak** did manage to identify the split-vacancy ground-state for V_{Sb} in Sb_2O_5 , lower in energy by ~ 1.5 eV and significantly impacting doping concentrations, when using large bond distortions and atom rattling. Here, the lower symmetry and reduced coordination of Sb in Sb_2O_5 compared to Ga_2O_3 is likely key to aiding split-vacancy identification, giving a lower energy barrier to the transformation which allows it to be identified with semi-local structure searching.

In this work, I set out to investigate the prevalence of split vacancies in solid-state compounds. Currently only a small handful of these species, mentioned above, are known. Is this the result of their rarity in nature, or simply because we have not had the computational tools to efficiently search for these species (or both)? Indeed the prevalence of defect metastability in general is more appreciated due to recent efforts for efficiently identifying this behaviour.^{9,11,20,42–45,48} The goal of this work is thus to understand the driving factors for split-vacancy defect formation, and then leverage these insights to develop an efficient approach for their identification. Finally, I leverage the speed of this workflow to screen all compounds in the Materials Project database (which includes all entries in the Inorganic Crystal Structure Database (ICSD), along with several thousand computationally-predicted materials), identifying thousands of hitherto unknown split vacancy defects.

Results

Factors Driving Split Vacancy Formation

The identification of split vacancy structures is not, at first glance, trivial. Local structure-searching approaches, despite their general success, do not succeed in identifying these species in most known cases. A brute force enumeration approach, where each possible vacancy-

interstitial-vacancy combination (i.e. split vacancy) is trialled with a coarse total energy calculation – DFT or otherwise – is also out of the question. For instance, if we enumerate all possible symmetry-inequivalent $V_X\text{-}X_i\text{-}V_X$ complexes with $V_X\text{-}X_i$ distances less than 5 Å, with interstitial sites determined by Voronoi tessellation,^{12,49} this gives 540 combinations in $\alpha\text{-Ga}_2\text{O}_3$, 1267 in $\beta\text{-Ga}_2\text{O}_3$, 452 in Sb_2O_5 and even larger numbers in compounds with lower symmetry and/or greater multinarity. In most cases, it is infeasible to perform DFT supercell calculations for such a large number of trial structures, especially when considering each symmetry-inequivalent vacancy site and charge state.

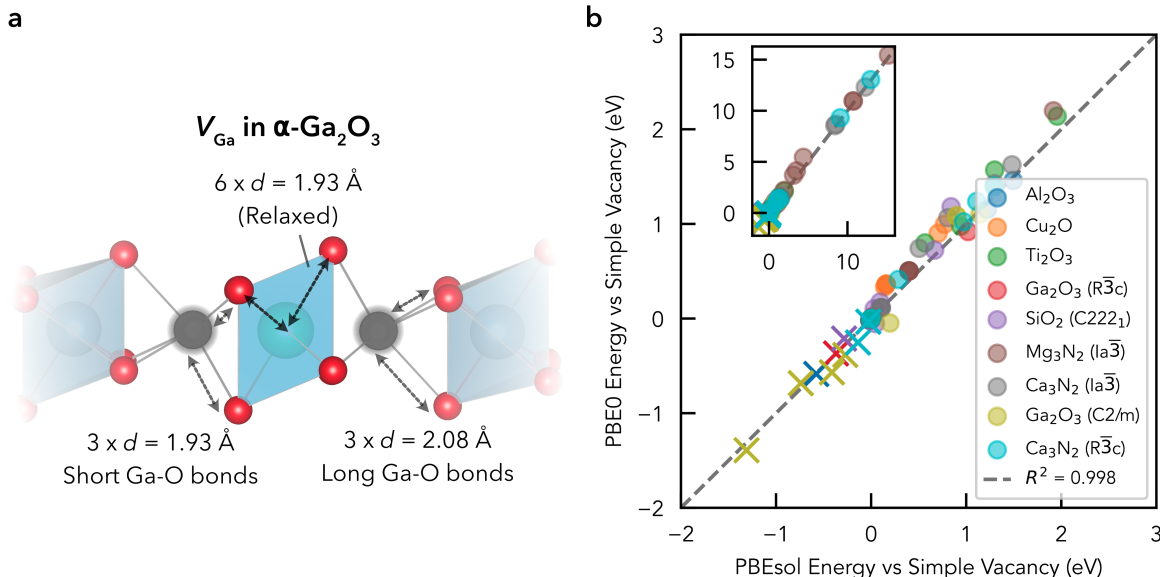


Figure 2. Geometric and DFT energy analysis of split vacancies. **(a)** Geometric analysis of the split vacancy for V_{Ga} in $R\bar{3}c$ $\alpha\text{-Ga}_2\text{O}_3$, indicating short and long cation-anion bond lengths. The interstitial cation within the split vacancy ($[V_X + X_i + V_X]$) is highlighted in lighter blue as in Fig. 1, and vacancy positions are indicated by the semi-transparent grey circles. **(b)** Energies of relaxed candidate split vacancy configurations relative to the lowest energy symmetry-inequivalent simple vacancy, using semi-local GGA (PBEsol; x -axis) and hybrid DFT (PBE0; y -axis). Split vacancies which are lower energy than the lowest energy simple vacancy are denoted by \times symbols, and the same plot over a wider energy range is shown inset. This dataset includes cation vacancies for oxides and the anion vacancy for nitrides (anti-corundum-like structures).

The efficient identification of split-vacancy clusters will thus require a significant reduction of this search space to a tractable number of candidate structures. In this regard, it is beneficial to understand the driving forces of their formation, in order to leverage these physical insights in our computational strategy. Here we take V_{Ga} ³ in the $R\bar{3}c$ corundum-structured $\alpha\text{-Ga}_2\text{O}_3$ phases as an example (shown in Fig. 1a) – for which the same split vacancy transformation is known to occur in the isostructural $\alpha\text{-Al}_2\text{O}_3$ (sapphire).¹² As shown in Fig. 2a, each cation octahedron has three short ($\sim 1.93 \text{ \AA}$) and three long ($\sim 2.08 \text{ \AA}$) Ga-O bond lengths. In the simple vacancy we thus have three short and three long cation-anion dangling bonds, while in the split vacancy ($V_X \rightarrow V_X + X_i + V_X$) we instead have three long cation-anion dangling bonds for each of the two vacant octahedra. The formation energy of a defect is essentially derived from the energetic cost of the bond breaking and creation induced by its formation, and associated strain costs. Here, the breaking of only the *longer* cation-anion bonds is found to result in a more energetically favourable arrangement than breaking both *short* and *long* cation-anion bonds. While not entirely straightforward due to the lower symmetry and variable preferences for shorter/longer cation-anion bond lengths, the connection between simple bond counting

and the energetic ordering of simple vs split vacancies here suggests that their formation can be estimated through analysis of the host crystal structure. In particular, the existence of the low energy split (cation) vacancy evidently requires an interstitial position located adjacent to two cation sites, which has similar (or greater) anion coordination compared to the host cation site.

Table 1. Energies in electronvolts (eV) of split vacancy configurations relative to the lowest-energy symmetry-inequivalent simple vacancy, in known occurrences.^{12,14,19,30,47}. Relative energies calculated using both the semi-local PBEsol and hybrid non-local PBE0 DFT functionals are given. Asterisks (*) denote metastable split-vacancy configurations, for cases where there are multiple symmetry-inequivalent low-energy split vacancy states.

Functional	Al ₂ O ₃ <i>R</i> $\bar{3}c$ V_{Al}^{-3}	Ga ₂ O ₃ <i>R</i> $\bar{3}c$ V_{Ga}^{-3}	Ga ₂ O ₃ <i>C</i> 2/ <i>m</i> V_{Ga}^{-3}	Ga ₂ O ₃ <i>C</i> 2/ <i>m</i> V_{Ga}^{-3*}	Ga ₂ O ₃ <i>C</i> 2/ <i>m</i> V_{Ga}^{-3**}	SiO ₂ <i>C</i> 222 ₁ V_{Si}^{-4}	Ca ₃ N ₂ <i>R</i> $\bar{3}c$ V_{N}^{+3}	Sb ₂ O ₅ ^[2] <i>C</i> 2/ <i>c</i> V_{Sb}^{-5}
PBEsol	-0.58	-0.37	-1.31	-0.74	-0.41	-0.28	-0.14	-1.43
PBE0	-0.59	-0.37	-1.39	-0.68	-0.57	-0.21	-0.25	-1.47

[2] For Sb₂O₅, the listed values correspond to the energy differences between the ground and metastable split vacancy states, as the PBEsol simple vacancy V_{Sb}^{-5} geometry destabilises during PBE0 relaxation, making the split vs simple vacancy comparison invalid for this case.

Taking a selection of the known cases of (meta)stable split vacancy defects, discussed in the introduction, I calculate the relative formation energies of the split and simple vacancy configurations using both hybrid DFT (PBE0) and semi-local GGA DFT (PBEsol), and tabulate the results in Table 1. In most cases, there is good agreement between hybrid and semi-local DFT for the relative energies, between split and simple vacancy configurations, as well as between metastable split vacancy states. This is further demonstrated in Fig. 2b, where we see high correlation ($R^2 = 0.998$) between the PBEsol and PBE0 relative energies for these defects. At first, this may seem surprising, as semi-local DFT is notoriously inaccurate for calculating defect formation energies in semiconductors and insulators. Indeed, we have tested if defect structure-searching with **ShakeNBreak**⁴² could be performed using semi-local DFT to identify distinct stable defect geometries, before using higher-level theories to relax and compute energies with greater accuracy, but found that it was unable to even *qualitatively* identify ground-state defect geometries in around 50% of the reconstructions (missed by standard relaxations) reported in Mosquera-Lois *et al.*⁹ – let alone give reasonable estimates of relative energies. In each case, this error could be attributed to either self-interaction and resulting spurious delocalisation errors inherent to semi-local DFT (inhibiting charge localisation, which often drives these structural reconstructions) or the related band gap underestimation (spuriously destabilising certain defect charge states).^{46,49,50} However, this is not the case for *fully-ionised* defect charge states,^[3] where there is no excess charge and so no requirement for charge localisation to stabilise the defect. In these cases, the main contributors to formation energies are typically cohesive energies (i.e. bond breaking energies) and electrostatic effects.

[3] Fully-ionised charge states refer to the case where all atoms are assumed to be in their formal oxidation states, and so e.g. in Al₂O₃ addition of an O⁻² anion to create an interstitial would give O_i⁻², substitution of an oxygen site with aluminium would give Al_O⁺⁵, removal of an Al⁺³ cation to create a vacancy would give V_{Al}^{-3} etc. Fully-ionised charge states are often the most stable charge states for defects in semiconducting and insulating solids.

This is additionally why fully-ionised defect species tend to show *less* structural reconstructions than other charge states,^[4] as the lack of excess charge to localise results in less degrees of freedom in the defect geometry energy landscape, with ionic rather than covalent interactions dominating. The lack of charge localisation and dominance of ionic interactions in the formation of fully-ionised defect species means that semi-local DFT often performs adequately in computing the formation energies of these defects, without the need for improved exchange-correlation descriptions from hybrid DFT.^{12,46} It is important not to misinterpret this point, semi-local DFT will fail miserably in the vast majority of cases beyond fully-ionised defect states, which are usually only a subset of the relevant defects in a given material. Indeed, this can be seen from the results of Kononov *et al.*¹² for defects in $R\bar{3}c$ α -Al₂O₃ (a.k.a. sapphire), where the relative energies of various defect configurations in different charge states were calculated with both semi-local (PBE) and hybrid DFT (HSE06), with poor agreement for non-fully-ionised charge states, but excellent agreement ($\Delta = 0.02$ eV) for split-vacancy V_{Al}^{-3} . Split vacancies have mostly only been reported for defects in their fully-ionised charge states (Table 1), and so we see that semi-local DFT is in most cases sufficient to describe the energetic preference for split over simple vacancies in these cases.

Combined, the above considerations indicate that electrostatic and strain effects are the key driving factors for split vacancy formation in solids, with charge localisation and covalent bonding having minimal impacts. This suggests that consideration of cation-anion bonding in simple vs split vacancy configurations could be used to estimate the preference for split vacancy formation, prior to full quantum-mechanical calculation. With this in mind, I trial a simple electrostatic model using an Ewald Summation to compute Madelung energies, assuming all ions are in their formal charge states (i.e. fully-ionised charge states) and adding a compensating background charge density to avoid divergence, as implemented in the `pymatgen EwaldSummation`^{52,53} tool. Fig. 3a shows the distribution of these electrostatic energies for all possible symmetry-inequivalent $V_{\text{X-X}_i}$ - V_{X} complexes, with $V_{\text{X-X}_i}$ distances less than 5 Å and interstitial sites determined by Voronoi tessellation (example in Fig. 4),^{12,49} for a selection of compounds which have previously been investigated for split vacancy formation.^{12,14,33,47} I note that the electrostatic energy range here is quite large due to the use of formal oxidation states for the ionic charges (i.e. neglecting screening, which would require prior DFT / electronic structure calculations), however this should not affect the qualitative trends. We also witness wider energy ranges for more highly-charged systems (e.g. Sb^{+5} in Sb_2O_5 vs Cu^{+1} in Cu_2O) as expected. This approach yields a wide set of candidate geometries, the vast majority of which have highly-unfavourable electrostatic energies. However, we see that in each compound with split vacancies *lower* in energy than any simple point vacancy, the corresponding initial $V_{\text{X-X}_i}$ - V_{X} geometries (denoted by \times symbols) have electrostatic energies close in the minimum tail of these broad distributions, indicating that this relatively cheap electrostatic calculation can be used to screen for candidate low energy split vacancies effectively. If we take as a screening cut-off value the electrostatic formation energy of the lowest energy simple vacancy (i.e. the electrostatic energy of the simple vacancy minus that of the pristine bulk supercell), plus 10% to account for energy shifts due to strain and relaxation effects, we see that the identified lower energy split vacancies are well captured by this range (indicated by the short black horizontal lines in Fig. 3a). This vacancy-dependent cut-off gives between 2 and 8 candidate split vacancy geometries in each case, with an average of ~ 4 , corresponding to a tiny subset of the ~ 500 possible $V_{\text{X-X}_i}$ - V_{X} configurations each.

This correlation between the electrostatic and DFT energies is further demonstrated in Fig. S3 for the initial test set and in Fig. 3b for all semi-local DFT calculations performed in this study. We see that low electrostatic energies mostly correspond to low DFT energies (though with the neglect of strain, pair repulsion and covalent bonding still yielding significant spread),

[4] Of the reconstructions we do find for fully-ionised defects, many are for interstitials where the ionised interstitial moves to a site with lower electrostatic and strain energies, similar to the behaviour of split vacancies here.^{4,9,51}

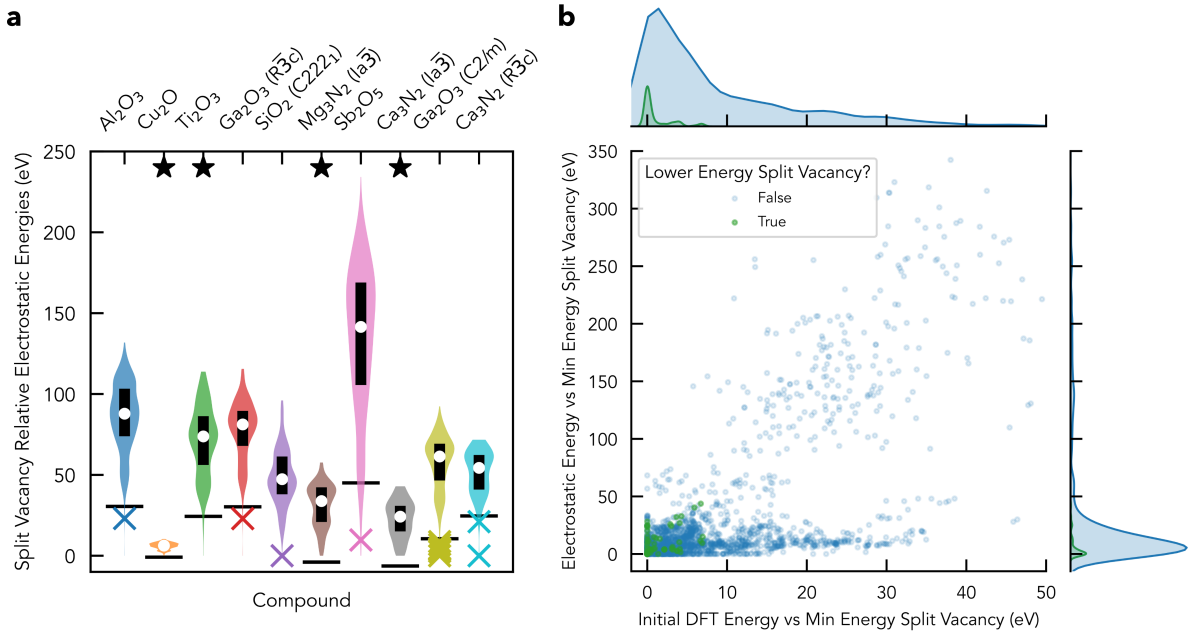


Figure 3. Electrostatic and DFT energy distributions of investigated vacancy structures. **(a)** Violin distribution plots of the relative electrostatic energies of candidate $V_X\text{-}X_i\text{-}V_X$ complexes, with $V_X\text{-}X_i$ distances less than 5 Å and interstitial sites determined by Voronoi tessellation,^{12,49} across the same initial compound test set as Fig. 2b (V_{Cation} for oxides and V_{Anion} for nitrides). There are ~ 500 candidate configurations in each set. White circles and black rectangles denote the median and interquartile range respectively. Short horizontal black lines indicate the chosen cut-off energy for further screening, corresponding to the 110% of the electrostatic formation energy of the lowest energy simple vacancy. As in Fig. 2b, split vacancies which are lower energy than the lowest energy simple vacancy are denoted by \times symbols. Compounds which do not show lower energy split vacancy geometries are indicated with black stars. **(b)** Joint distribution plot of the (initial) electrostatic energies of all candidate split vacancies in the full DFT calculated dataset (~ 1000 compounds) against their corresponding (initial) DFT energies, relative to the minimum energy candidate split vacancy geometry in both cases. ‘Initial’ refers to the fact that these energies are computed for candidate split vacancies before performing geometry relaxation (as in the electrostatic screening step). Configurations which relax to split vacancies which are lower energy than the lowest energy simple vacancy are highlighted in green.

and initial geometries yielding lower energy split vacancies corresponding to those with low electrostatic energies (and low initial DFT energies). While the initial DFT energies of these configurations, prior to relaxation, are themselves not a perfect indicator of final *relaxed* relative energies, we do see that they provide a decent estimate of relative stabilities, as indicated by the joint distribution plot of initial and final (pre- and post-relaxation) energies in Fig. S4, and fact that all identified lower energy split vacancies in Fig. 3b have low initial DFT energies. This is exemplified by the case of V_{Sb}^{-5} in Sb_2O_5 in Fig. 4, which shows the initial and final (relaxed) DFT and electrostatic energies of the simple point vacancy and 2 of the 10 candidate $V_X\text{-}X_i\text{-}V_X$ complexes predicted. Here the initial electrostatic energies do not perfectly correlate with the DFT energies, but are effective in reducing the search space by identifying low *electrostatic energy* configurations which may yield low *total energies* upon relaxation. While not perfectly precise, we see that this simple geometric and electrostatic approach allows us to rapidly screen through hundreds of possible $V_X\text{-}X_i\text{-}V_X$ configurations for each candidate vacancy and reduce this to a small handful of candidate geometries which are then tractable for DFT energy evaluation – particularly given the demonstrated accuracy

of cheaper semi-local DFT for these specific fully-ionised defects.

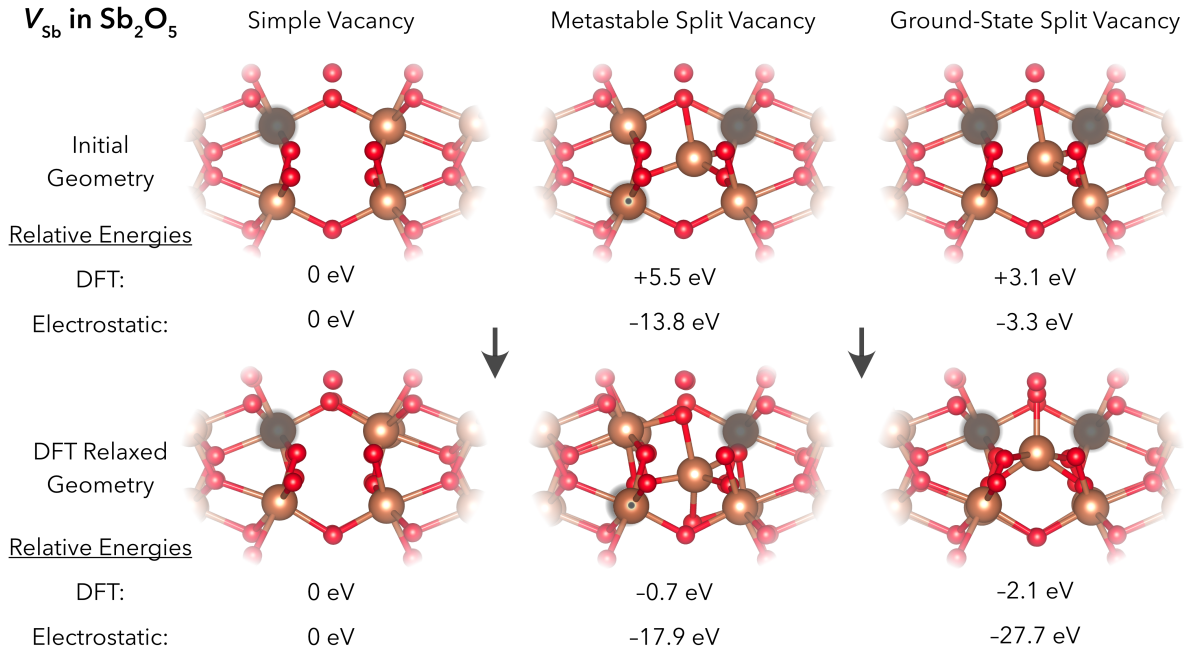


Figure 4. Low energy vacancy configurations in Sb_2O_5 , before and after DFT relaxation. The relative energies according to DFT (PBEsol) and an electrostatic model (assuming formal ionic charges, inflating magnitudes) are shown alongside, with the simple point vacancy set to 0 eV in each case. Vacancy positions are indicated by the semi-transparent grey circles.

Screening Split Cation Vacancies in Oxides

With this efficient computational model for estimating split vacancy formation, I apply a high-throughput screening approach to identify split cation vacancies in metal oxides, as illustrated in Fig. 5a. Oxides are used in a wide variety of materials applications, such as transparent conducting oxides (TCOs), power electronics, battery cathodes, heterogeneous catalysis and more, for which defects play crucial roles. Cation vacancies are typically the dominant acceptor defects in oxides,^{12,17,47,54,55[5]} thus playing key roles in electronic conductivity (counter-balancing the effects of positively-charged oxygen (anion) vacancies), ion diffusion, catalytic activity, optical properties and more. To this end, I apply this screening workflow to the database of ~ 1000 stable insulating metal oxide compounds previously investigated by Kumagai *et al.*⁴⁶ for their oxygen vacancy properties.

I first generate all symmetry-inequivalent $V_X-X_i-V_X$ ($X = \text{cation}$) complexes with V_X-X_i distances less than 5 \AA using *doped*, prune to only those with electrostatic formation energies $\leq 110\%$ of the lowest energy simple vacancy (with a maximum of 10 per cation vacancy), and then calculate this subset with the PBEsol semi-local DFT functional, matching the calculation parameters used in the original database generation.⁴⁶ Taking the first 444 metal oxide compounds in this database (comprising 992 possible cation vacancies), sorted by supercell size to optimise computational efficiency, this gives 183,000 possible $V_X-X_i-V_X$ geometries, which is reduced to 3,900 using the electrostatic screening criterion (595 cation vacancies in 396 compounds). This approach reveals 93 lower energy cation vacancies, corresponding to

[5] Outside of mixed-cation oxides with chemically-similar heterovalent cations.^{13,25,56,57}

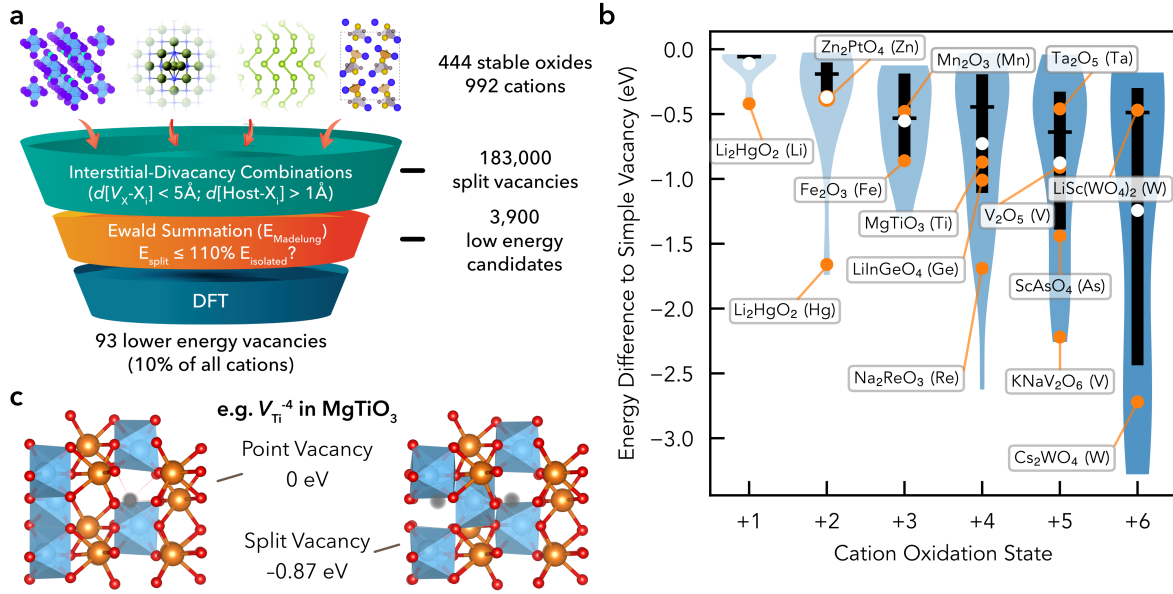


Figure 5. Screening split cation vacancies in metal oxides. **(a)** Schematic diagram of the initial screening workflow employed to identify split cation vacancies in stable metal oxide compounds. 93 lower energy cation vacancies are identified, corresponding to $\sim 10\%$ of all possible cation vacancies, and $\sim 20\%$ of cation vacancies with at least one low electrostatic energy $V_X-X_i-V_X$ arrangement. **(b)** Distribution of split vacancy energies relative to the lowest energy symmetry-inequivalent point vacancy for different cation oxidation states, for all lower energy split cation vacancies in metal oxides identified in this work ($\Delta E < -0.025$ eV). Some example compounds and the corresponding cation (vacancy) are shown as labelled orange datapoints. White circles, black dashes and rectangles denote the mean, median and inter-quartile range respectively. **(c)** Example of DFT-relaxed point vacancy and split vacancy structures for V_{Ti}^{-4} in MgTiO_3 , with Ti in blue, Mg in orange, O in red and vacancies as semi-transparent grey circles. Only Ti polyhedra are shown for clarity.

$\sim 10\%$ of possible cation vacancies in this dataset, with energy differences to the lowest energy simple point vacancy between 0.05 and 3 eV (Fig. 5b), with a mean energy lowering of 0.81 eV. Using a distance-based classification algorithm implemented in `doped`⁴⁹ (Section S2), just over 50% of the lower energy vacancies are determined to form split-vacancy type geometries like that shown in Fig. 5b, while the others rearrange to adopt distorted point vacancy structures which are lower energy than those obtained from standard geometry relaxations of the simple point vacancies. These are significant energy differences, with the mean energy lowering $\Delta E = 0.81$ eV amounting to over 3 orders of magnitude difference in equilibrium defect concentrations for a growth temperature of $T \sim 1000$ K, or 10 orders of magnitude in equilibrium populations at room temperature (relevant for charge compensation).

Moreover, this screening identifies many low-energy metastable states (e.g. as for Sb_2O_5 , Fig. 4), finding 300 (210) distinct metastable states with energies within 0.5 eV of the lowest energy simple point vacancy, in 200 (160) of the 600 cation vacancies which gave candidate low-energy sites from electrostatic screening in this test set, with distributions and tabulated data provided in Section S5. Here I classify distinct metastable states as those which (i) relax to a split vacancy geometry (determined by the `doped`⁴⁹ classification algorithm), with no corresponding symmetry-inequivalent point vacancy spontaneously relaxing to a split vacancy, or have a difference in energy > 50 meV to any corresponding symmetry-inequivalent point vacancy (well above the energy noise in these calculations), and (ii) are different in energy by > 25 meV to all other metastable states for that vacancy. Numbers in parentheses are when *only* split vacancy geometries are included. Identification of low-energy metastable

states for defects in solids is important for understanding a number of key defect properties, such as carrier recombination rates,^{10,15,16,23,24} oxidation and decomposition,^{13,25} catalytic activity,^{26,58,59} field-effect transistors⁶⁰ and more.^{33,48} Many of these compounds which exhibit lower energy split vacancies are being investigated for functional materials applications where defect behaviour is crucial, such as MgTiO₃ which is used in wireless communication for its excellent dielectric properties (Fig. 5c),^{61,62} CsReO₄ for potential applications in photocatalysis and radioactive waste storage,⁶³ Ta₂O₅ for oxygen evolution reaction (OER) catalysis,^{64,65} Fe₂O₃ for photoelectrochemical water oxidation,^{66,67} and V₂O₅ for high capacity battery electrodes.^{68,69} For instance, the preference for Co/Ni migration to interlayer positions in delithiated Li_{1-x}(Co, Ni)xO₂ cathode materials, known to drive degradation and capacity fade,^{13,70,71} is predicted here – corresponding to split Co/Ni vacancies in fully-delithiated Li_{1-x}(Co, Ni)xO₂. It is imperative that the correct ground states and low-energy metastable states are identified in defect investigations of these compounds, as these large energy differences and distinct geometries could drastically affect predictions.

From these results, we can conclude that split vacancy defects do have a significant prevalence across different materials and structure types, and are not just limited to the handful of known cases discussed in the introduction (mostly (anti-)corundum structures). As expected, larger cation oxidation states give larger ranges of energy lowering, corresponding to stronger electrostatic bonding and thus greater magnitudes of energy variations from different ion arrangements (matching the trends in electrostatic energy ranges in Fig. 3a). These large energy-lowering reconstructions for negatively-charged cation vacancies in oxides will make these acceptor defects much shallower, yielding greater compensation of any *n*-type doping – typically from oxygen vacancies.⁴⁶ These lower energy geometries are also expected to inhibit cation migration, having increased energy barriers to displacement away from the equilibrium geometries, as for Ga₂O₃.^{17,33}

Machine Learning Acceleration

From the above results, we see that this geometric and electrostatic pre-screening model greatly reduces the search space for split vacancy configurations in solids, allowing the screening and identification of these species in several hundred metal oxides. This once again highlights that the primary contributions to low energy split vacancy formation are electrostatic effects, with the remaining inaccuracies (prior to DFT computation) stemming from strain, pair repulsion and remnant covalent bonding effects which are not captured by this simple model. These considerations hint at the possibility of using some form of simple energy potential to estimate these contributions to further improve the accuracy and thus efficiency of this pre-screening approach. Machine-learned force fields (MLFFs) – machine learning models trained on energies and forces from quantum-mechanical simulations – present an attractive option for this goal. In particular, ‘foundation’ MLFFs (a.k.a. universal potentials) are trained on large and diverse datasets of DFT simulations, affording generality to these models (applicable to compositions spanning the periodic table) and achieving accuracies close to that of semi-local DFT but at a small fraction of the computational cost.^{72–74}

Here, I take the MACE-mp foundation model,^{72,75} which is an equivariant graph neural network force field trained on semi-local DFT (PBE) geometry relaxations for inorganic crystalline solids in the Materials Project database.⁷⁶ Using this universal potential to relax all split vacancy candidate geometries in the metal oxides test set discussed above, I find that it successfully predicts the energetic preference for split vs simple vacancies in 88.1% of the ~600 cation vacancies calculated with DFT. Inaccuracies in the foundation model predictions are more concentrated in cases where split vacancies are the *lowest* energy geometry however, with MACE-mp correctly predicting the split vacancy state for 53% of the energy-lowering split vacancies subset. If we take a more exhaustive approach, where we consider all distinct MACE-mp-relaxed split vacancy geometries (via the doped classification algorithm) with energies within 0.35 eV of the ground state as candidate lower energy states (to maximise our

Table 2. Performance metrics for MACE-mp foundation models in identifying split vacancy configurations for the test set of cation vacancies in metal oxides (Fig. 5), with candidate geometries from geometric & electrostatic screening as input. The prevalence rate of cation vacancies for which a split vacancy is the lowest energy state (with $\Delta E < -25$ meV) is 8 %, while that of *candidate geometries* which result in the lowest energy state is 0.7 % – the latter indicated by ‘prevalence*’ here. F1 score is a common metric used for ML classification methods, while the ‘discovery acceleration factor’ (DAF) quantifies the speedup in discovery (of split vacancies in this case) compared to random selection.⁷³ DAF has a maximum value of 1/Prevalence for perfect accuracy, which corresponds to 12.5 and 143 for DAF*. For TPR/FPR/TNR/FNR; T = True, F = False; P = Positive, N = Negative; R = Rate. The definitions of the various metrics are given under their title. ‘Small’ refers to the MACE-mp-small model, while ‘exhaustive’ is when ML-predicted metastable split vacancies with $\Delta E < 0.35$ eV) are included (see text). Champion values shown in bold.

Model	F1	Precision	DAF	DAF*	TPR	FPR	TNR	FNR
	$\frac{TP}{TP+(FP+FN)/2}$	$\frac{TP}{TP+FP}$	$\frac{\text{Precision}}{\text{Prevalence}}$	$\frac{\text{Precision}}{\text{Prevalence}^*}$	$\frac{TP}{TP+FN}$	$\frac{FP}{FP+TN}$	$\frac{TN}{TN+FP}$	$\frac{FN}{FN+TP}$
small	0.63	0.78	9.76	118.9	0.53	0.01	0.99	0.47
exhaustive	0.56	0.43	5.33	64.9	0.81	0.09	0.91	0.19

true positive hit rate, at the cost of some efficiency (i.e. false positives)), this gives a model which correctly identifies the split vacancy state for 81 % of our energy-lowering split vacancies subset. The performance metrics of the best models are tabulated in Table 2, showing that the best performing models achieve F1 scores around 0.6 (a commonly-used ML classification metric), ‘discovery acceleration factors’ (DAF) up to ~ 10 (which represents the speedup in discovery, of lower energy split vacancies in this case, provided by the ML model, with a maximum value of $1/\text{Prevalence} \simeq 12.5$)⁷³ and true positive rates (TPR) up to 81 %.

The high DAF values here demonstrate the significant speedup offered by the ML foundation model in identifying low energy split vacancies. Given that I only take the lowest energy split vacancy predicted by the ML model (rather than all candidate geometries from the electrostatic screening step, with an average of 12.2 per cation vacancy), the actual acceleration factor in terms of numbers of DFT calculations to perform is $\text{DAF}^* = 118.9$, giving over two orders of magnitude speedup. Moreover, these discovery metrics are based on the prevalence of lower energy split vacancies within the electrostatically-screened geometries, and so the actual DAF compared to random selection of all possible $V_X\text{-}X_i\text{-}V_X$ geometries would be orders of magnitude larger. Applying the ‘small’ model to the remaining fraction of the metal oxides dataset⁴⁶ and then using DFT to compute the energies of predicted lower energy split vacancies, relative to the symmetry-inequivalent point vacancies, I find that it successfully predicts a *lower* energy split vacancy in 44 % of cases. Notably, the majority of ‘false positives’ here do retain split vacancy geometries, adopting low energy metastable states which are still relevant to defect investigations as discussed above.^{14,33,48} I note that a number of model choices, such as model size, floating point precision, geometry optimisation algorithm and more, were tested for this step in the workflow, as detailed in the Methods and Section S4.

This predictive ability of the foundation ML model, on top of the geometric and electrostatic screening step, allows a tiered screening procedure to estimate the formation of low energy split vacancies with high efficiency, making it applicable to extremely large datasets of materials. As depicted in Fig. 6, I use this approach to search for split cation vacancies in all compounds on the Materials Project (MP) database, which includes all entries in the ICSD (as of November 2023), along with several thousand computationally-predicted metastable materials.⁷⁶ With this screening procedure, the ML model predicts lower energy structures missed by standard defect relaxations for $\sim 56,000$ cation vacancies (or 20 % out of a total pool

of $\sim 280,000$ within this dataset) in 44,000 materials, of which 32,000 (11%) are classified as split vacancies.⁴⁹ To test the accuracy of this approach, and investigate the prevalence of split cation vacancies within a different chemical subspace, I take all cases of ML-predicted lower energy split vacancies in nitride compounds which are thermodynamically-stable (according to MP calculations) and do not contain lanthanides (which can be poorly modelled by standard DFT), and again compute the energies of predicted lower energy split vacancies relative to the symmetry-inequivalent point vacancies using DFT, matching the MP computational setup. Here the ML model predicts 198 (103) cation vacancies with lower energy structures, while DFT shows this to be true in 113 (40) cases, corresponding to a predictive accuracy of 57% (39%) here – values in parentheses corresponding to those where relaxed geometries are classified as split vacancies. The slightly worse predictive accuracy for nitrides (39%) compared to oxides (44%) is likely a result of the greater prevalence – and thus expected accuracy for – oxides in the MPTrj dataset upon which MACE-mp is trained.⁷³ If we take the lower-bound predictive accuracy of $\sim 40\%$ from our oxide and nitride test sets, this would correspond to $\sim 22,000$ (13,000) lower energy cation vacancy structures being identified by the electrostatic + ML screening of the MP database, and around 60% more if we employ the ‘exhaustive’ model.

Analysing the distributions of DFT-confirmed low energy split cation vacancies in metal oxides, no clear trends are seen for the host compound space groups, however we do see a trend if we look at the point symmetry of the candidate split vacancy. Fig. 6b shows that higher symmetry geometries, as measured by the point group order of the X_i site in the $V_X-X_i-V_X$ geometry, correlate with a higher prevalence of low energy split vacancies. This is likely due to higher symmetry sites corresponding to greater cation-anion bonding and more bulk-like coordination, favouring lower energies as seen in the example cases discussed in the introduction. Fig. 6c shows that certain cations have particularly high prevalences of predicted lower energy split vacancies, such as cationic carbon, chalcogens, halogens, hydrogen, magnesium, mercury, vanadium and coinage metals (Cu, Ag, Au). Looking at host compound compositions (Fig. 6d), we see that compounds with nitrogen, carbon, magnesium, bromine, osmium and mercury have high prevalences of predicted lower energy split vacancies, while prevalence rates decrease on average as we move down the periodic table.

Discussion & Conclusions

The identification of ground and metastable configurations is crucial to our understanding of defects in materials. The defect geometry is the foundation from which its behaviour and associated properties (such as formation energy, concentration, migration, doping etc) derive, and is thus key to both experimental and theoretical characterization of defects. For instance, some key impacts of split cation vacancy formation are the increased acceptor defect concentration (due to the significant lowering of the cation vacancy (dominant acceptor) formation energies), yielding greater compensation of oxygen vacancy donors and impacting the migration of highly-charged defects under strong electric fields.^{17,33} The importance of energy-lowering reconstructions from simple, unperturbed defect geometries to key material properties has been demonstrated in a wide range of materials and applications in recent years, aided by improved structure-searching methods,^{9,11,42–45} however ‘non-local’ defect reconstructions such as split vacancies remained elusive. We see that these defect species are present in significantly more materials than previously known, with prevalence and importance varying as a function of composition, point symmetries and oxidation states. This once again highlights the importance of advanced global optimisation methods for defects which can accurately and efficiently scan their potential energy surfaces, to identify which defects are actually present.¹¹

To rapidly assimilate the findings of this study to a directly usable form for the defect community, this database of screened split vacancy configurations in known inorganic solids has been made directly accessible through the `doped`⁴⁹ defect simulation package [**private branch to be released upon publication**]. `doped` automatically queries this database upon defect

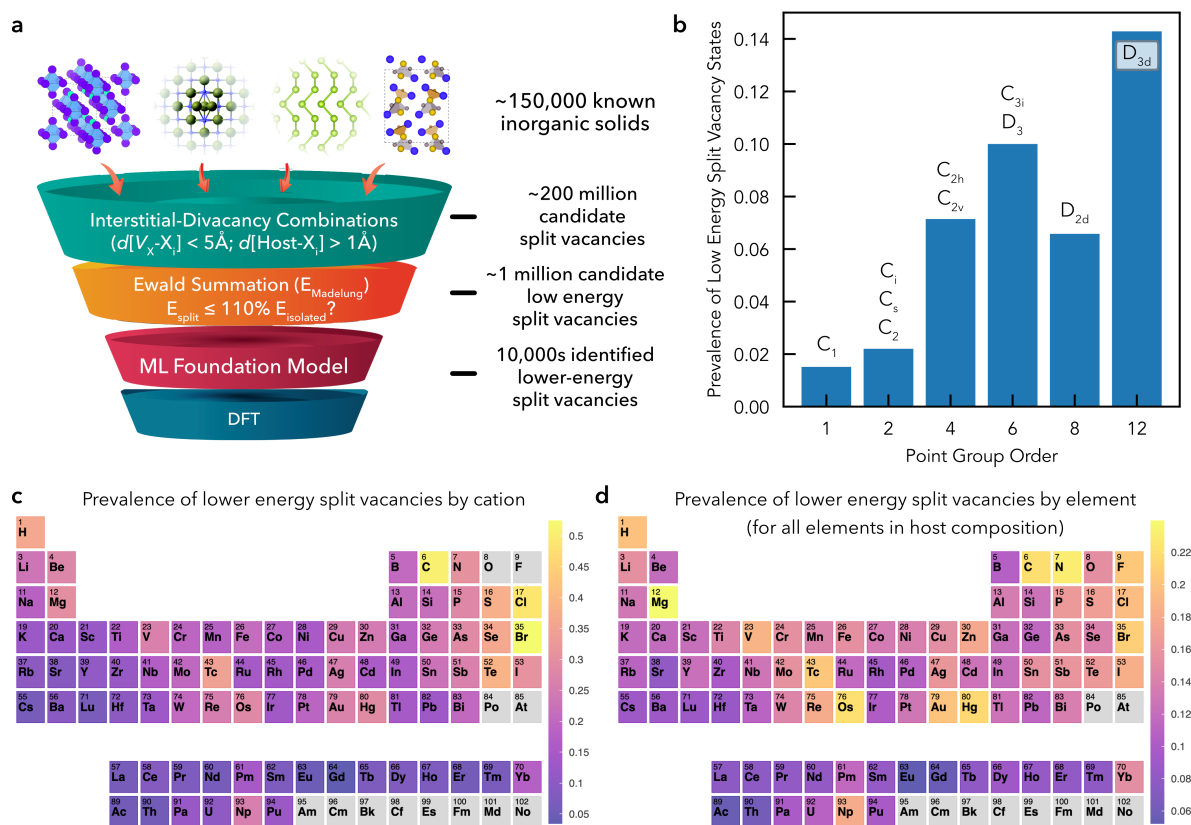


Figure 6. ML-accelerated screening of split vacancies. **(a)** Schematic diagram of the ML-accelerated screening workflow employed to predict the formation of split cation vacancies in all compounds in the Materials Project⁷⁶ (MP) database. **(b)** Normalised prevalence of distinct low-energy split vacancies within the electrostatically-screened set of candidate $V_X-X_i-V_X$ geometries for all cation vacancies in metal oxides computed with DFT, as a function of the point group order of the X_i site (as given by the *doped*⁴⁹ defect symmetry functions). Values are normalised by the total prevalence of each point group within the electrostatically-screened set of candidate X_i . The point group order corresponds to the number of symmetry operations, with higher order corresponding to higher symmetry. **(c,d)** Heatmap plots of the normalised prevalence of lower energy split vacancy states predicted by the ML-accelerated screening of the MP database, for **(c)** the cation vacancy element and **(d)** all elements in the corresponding host compound. Values are normalised by the total prevalence of each element within the dataset. The same heatmaps, weighted by energy lowering magnitudes and using logarithmic colourbar scales, are provided in Fig. S10.

generation, informing the user if low energy split vacancies are predicted for the input host compound, and at what level of confidence. This will allow defect researchers to easily and automatically incorporate the behaviour of low energy and metastable split vacancies in future studies, without the need to perform advanced structure-searching, boosting the accuracy of our predictions as a community. Moreover, all code used to generate and screen candidate split vacancies, using *doped*,⁴⁹ *pymatgen*,⁵³ *vise*,⁴⁶ *ASE*,⁷⁷ and *MACE*⁷⁵, along with the full database of predicted structures and confidence of low energy split vacancy formation is openly available at <https://doi.org/10.5281/zenodo.XXXX> [released upon publication]. The individual functions to implement each step in the structure-searching and screening approach from this work are likewise implemented in *doped*⁴⁹, so that users can predict the formation of split vacancies in novel compounds not listed on the Materials Project⁷⁶ database, make use of future ML models with improved accuracy or efficiency for screening, or examine the

possibility of other low-energy complex defects with a similar approach.

It is worth noting that these split vacancies are essentially a stoichiometry-conserving defect complex; V_X - X_i - V_X ; rather than a true ‘point defect’, which raises some general questions and considerations for their interpretation. For instance, their multiplicity and degeneracy pre-factors (Ng) in the defect concentration equation ($N_X = Ng \exp(-\Delta E/k_B T)$) will in most cases be reduced from that of the simple point vacancies. In α - Al_2O_3 for example, there is only one split-vacancy configuration per 2 host Al sites (i.e. possible simple vacancy sites), reducing its multiplicity pre-factor by half.^{2,23[6]} Indeed often the energy-lowering reconstructions we observe for point defects can be thought of as effectively ‘defect clusters’ rather than true point defects. For instance, the famous original cases of ‘DX-centres’ correspond to substitutional defects Y_X displacing significantly off-site, effectively transforming to interstitial-vacancy complexes Y_i - V_X .^{9,22,27,51,78} We have seen similar energy-lowering reconstructions to stoichiometry-conserving defect clusters in many cases with **ShakeNBreak**,^{9,42} such as the formation of dimers and trimers at vacancies chalcogenides and oxides^{13,27,47,51,79} as neighbouring under-coordinated atoms displace toward the vacant site in essentially $V_X \rightarrow V_Y + Y_X$ transformations. Advanced methods for identifying and characterising these defect clusters, similar to the vacancy classification algorithms used in Kumagai *et al.*⁴⁶ and in this work, will improve our understanding of the prevalence and typical behaviours of such defect clusters.

The workflow introduced here could be effectively applied to screen for other low-energy defect complexes in solids, both stoichiometry-conserving and otherwise. Defect complexes typically involve fully-ionised constituent point defects and are mostly governed by electrostatic attraction and strain,⁸⁰ as was shown to be the case for split vacancies here. As such, they correspond to a similar computational problem of large configuration spaces but with relatively simple energetics, for which we see that geometric, electrostatic and universal MLFF screening can be powerfully applied. For instance, most single-photon emitters or ‘quantum defects’, with applications in quantum sensing, communication and computing, are complex defects such as the NV centre in diamond⁸¹ or the T centre in silicon.⁸² Indeed, efforts have already begun to computationally screen thousands of candidate quantum-active complex defects to identify high-performance colour centres,⁸² for which the screening approach and code introduced here could be used to boost the efficiency and scope of such studies.

This work serves as an exciting early demonstration of the power and utility of foundation ML potentials (a.k.a. universal MLFFs), allowing us to greatly expand the scope, scale and speed of computational materials investigations. The non-locality and large configuration space (e.g. ~ 500 candidate configurations per vacancy defect) for these split vacancy defects presents a significant challenge for their identification. However, the fact that the underlying energetic driving factors for their formation are relatively simple (primarily electrostatics and strain), despite this large configuration space, makes foundation MLFFs ideally suited to their identification. We see here that a general-purpose ML potential (MACE) is capable of predicting the formation of these species with reasonable accuracy. Only a minute fraction of the candidate structures from electrostatic screening of the MP⁷⁶ dataset would have been possible to evaluate with DFT, whereas the foundation ML model can predict their relative energies with reasonable qualitative accuracy in the space of a day – using a large number of GPUs.

Nevertheless, these exciting findings come with some important caveats. These foundation models *only* work so well here because the dominant bonding and energetics for these species are relatively simple, and do not involve carrier localisation, variable charges or excess charge (opposite to *most* defect species and metastabilities/reconstructions), for which they fail dramatically. Their power in this case stems from the combination of an enormous configuration

[6] These degeneracy factors are automatically computed and incorporated in thermodynamic analyses by **doped**.⁴⁹

space with underlying energetics that are well-reproduced by the foundation model. As such, this is a promising demonstration of the potential utility of machine learning (ML) approaches to defects and materials modelling in general, *when used appropriately*, but as a field we are still a long way away from having generally-applicable ML methods for defects.

Methods

The `doped`⁴⁹ defect simulation package was used extensively in this work, for the generation of symmetry-inequivalent defect sites, identification of candidate interstitial sites using Voronoi tessellation, supercell generation, geometric (distance) and symmetry analysis, DFT input file generation, utility functions for serialization and more. For interstitial generation, the default `doped` settings were used, with 0.9 Å as the minimum distance for candidate interstitial sites from the host atomic framework (`min_dist`), and 0.55 Å as the clustering tolerance (`clustering_tol`; interstitial sites separated by distances less than this value were combined as one candidate site, with preference for the higher symmetry site conditioned on the minimum distances to host atoms, controlled by `symmetry_preference`). As mentioned in the text, a distance-based classification algorithm was implemented in `doped` to classify simple, split and non-trivial vacancy geometries, detailed in Section S2. For the Ewald Summation electrostatic model, the dependence of candidate split vacancy relative energies on supercell size was tested, and found not to significantly affect energy differences for the supercell sizes used here (minimum periodic image distance of 10 Å).

All Density Functional Theory (DFT) calculations were performed within periodic boundary conditions through the Vienna Ab Initio Simulation Package (VASP).^{83–88} Using the projector-augmented wave (PAW) method, scalar-relativistic pseudopotentials were employed to describe the interaction between core and valence electrons.⁸⁹ For hybrid DFT calculations, the PBE0 hybrid functional was used.⁹⁰ For the initial test cases of known split vacancies (Table 1) and split cation vacancies in metal oxides (with host compounds taken from the database of Kumagai *et al.*⁴⁶), the PBEsol⁹¹ GGA DFT functional was used for the semi-local DFT calculations. Briefly, this metal oxides dataset comprises oxide compounds on the Materials Project^{76,46} which are predicted to be thermodynamically stable against competing phases, are dynamically stable with respect to Γ -point phonon modes (i.e. unit-cell-preserving distortions), have 4 or less symmetry-inequivalent oxygen sites, 30 or less atoms in their primitive cells (to avoid complex low symmetry structures), do not have multiple anions and do not have partially-occupied *d* or *f* orbitals. Further details on the compounds in this dataset are available in Ref. 46. Calculation parameters were set to be consistent with that used by Kumagai *et al.*⁴⁶ (using the `viso` package), avoiding the need for re-relaxation of the bulk lattice parameters, while also using some of the default relaxation settings in `ShakeNBreak`⁴² (real-space projections, energy convergence thresholds, force minimisation algorithm etc) which have been well-tested for their accuracy and efficiency for defect structure-searching.⁹ Here, this corresponded to the use of a plane-wave energy cutoff of 400 eV and Γ -point only sampling for the defect supercells (which ranged from 60 to 500 atoms in size), and a maximum atomic force convergence threshold of 0.01 eV/Å. For the stable nitrides test set, the PBE⁹² GGA DFT functional was used for DFT relaxations to match the Materials Project⁷⁶ computational setup, combining the `MPreLaxSet`⁵³ parameters with the default `ShakeNBreak`⁴² relaxation settings. This corresponded to the use of a plane-wave energy cutoff of 520 eV.

Random displacements of atomic positions (‘rattling’) to break symmetry can aid the identification of lower-energy, lower-symmetry geometries by gradient optimisers,^{9,42,43,45,46,93} however this did not significantly increase the number of lower energy split vacancies in this study, which is attributed to the fact that split vacancies mostly have high symmetries (Fig. 6b)¹⁴ and fully-ionised defects are much less likely to break symmetry.^{9–11,94} However, rattling did reveal some bulk phase transformations to lower-symmetry, lower-energy compounds (shakenbreak.readthedocs.io/en/latest/Tips.html#bulk

phase-transformations),^{93,95} which have imaginary phonon modes off the Γ point. These included Ta_2O_5 ($Pm\bar{m}n \rightarrow P2_1/m$; $\Delta E = 22$ meV/fu), $\text{TiTi}_2(\text{GeO}_3)_3$ ($P6_3/m \rightarrow P_1$; $\Delta E = 48$ meV/fu) and Li_5BiO_5 ($C2/m \rightarrow P2_1$; $\Delta E = 22$ meV/fu).

For the MACE-mp foundation model,⁷² both 32-bit and 64-bit float precisions were tested (Fig. S9), with 32-bit relaxed energies matching 64-bit to within a couple meV. 32-bit precision is $\sim 75\%$ faster on average, and so given the confirmed accuracy and speed this choice was used for MACE-mp relaxations. A number of tests of speed and accuracy for model size, optimiser algorithm and float precision were performed, with results shown in Section S4.

Periodic table heatmap plots were generated using the `periodic_trends`⁹⁶ script. Oxidation states were determined using the `doped` algorithms,⁴⁹ which first attempts to use a maximum *a posteriori* estimation approach with bond valences and ICSD oxidation states (as implemented in the `BVAnalyzer` class in `pymatgen`),^{53,97} then trialling the `pymatgen`⁵³ oxidation-state guessing functions (based on ICSD prevalences) if that fails. Of the $\sim 150,000$ compounds in the MP database, integer oxidation states are determined for $\sim 110,000$ compounds.

The screening approach employed here would not have been possible without several of the efficient algorithms in `doped`;⁴⁹ including fast geometric and symmetry analysis of complex structures (to determine symmetry-inequivalent defect sites and complexes), oxidation and charge state estimation, flexible generation parameters to maximise efficiency and reduce memory demands when screening thousands of complex compounds, and more. The stable generation of intrinsic and complex defects with reasonable estimated charge states in all compounds on the Materials Project,⁷⁶ including low-symmetry multinary compositions with large unit cells (> 200 atoms) such as $\text{Na}_{30}\text{Mg}_4\text{Ta}_{20}\text{Si}_{33}(\text{SO}_{48})_3$ and $\text{Na}_7\text{Zr}_2\text{Si}_5\text{Ge}_2\text{PO}_{24}$, was a powerful test of robustness.

Acknowledgements

I thank Irea Mosquera-Lois for a careful reading of this manuscript, valuable discussions regarding universal MLFFs, and for making useful parsing and plotting scripts²⁰ (and data) openly-available online. I acknowledge useful discussions with Dr Joel Varley regarding the performance of `ShakeNBreak` and other structure-searching strategies for split vacancy defects, Prof Beall Fowler regarding known split vacancy defects in solids, and Ke Li regarding split vacancies in Sb_2O_5 & Al_2O_3 . I would also like to acknowledge Prof Yu Kumagai for making his database of oxygen vacancy calculations in metal oxides openly-available online, which was used as an initial test set of compounds in this work. I thank the Harvard University Center for the Environment (HUCE) for funding a fellowship.

References

- [1] C. Freysoldt, B. Grabowski, T. Hickel, J. Neugebauer, G. Kresse, A. Janotti and C. G. Van de Walle, *Reviews of Modern Physics*, 2014, **86**, 253–305.
- [2] I. Mosquera-Lois, S. R. Kavanagh, J. Klarbring, K. Tolborg and A. Walsh, *Chemical Society Reviews*, 2023, **52**, 5812–5826.
- [3] F. Oba and Y. Kumagai, *Applied Physics Express*, 2018, **11**, 060101.
- [4] S. R. Kavanagh, R. S. Nielsen, J. L. Hansen, R. S. Davidsen, O. Hansen, A. E. Samli, P. C. Vesborg, D. O. Scanlon and A. Walsh, *Intrinsic point defect tolerance in selenium for indoor and tandem photovoltaics*, 2024, <https://chemrxiv.org/engage/chemrxiv/article-details/6706a93612ff75c3a1f8c995>.
- [5] M. E. Turiansky, A. Alkauskas, M. Engel, G. Kresse, D. Wickramaratne, J.-X. Shen, C. E. Dreyer and C. G. Van de Walle, *Computer Physics Communications*, 2021, **267**, 108056.
- [6] X. Zhang and S.-H. Wei, *Physical Review Letters*, 2022, **128**, 136401.

- [7] Y. Kumagai, S. R. Kavanagh, I. Suzuki, T. Omata, A. Walsh, D. O. Scanlon and H. Morito, *PRX Energy*, 2023, **2**, 043002.
- [8] D. C. Asebiah, E. M. Mozur, A. A. Koegel, A. Nicolson, S. R. Kavanagh, D. O. Scanlon, O. G. Reid and J. R. Neilson, *ACS Applied Energy Materials*, 2024.
- [9] I. Mosquera-Lois, S. R. Kavanagh, A. Walsh and D. O. Scanlon, *npj Computational Materials*, 2023, **9**, 1–11.
- [10] S. R. Kavanagh, A. Walsh and D. O. Scanlon, *ACS Energy Letters*, 2021, **6**, 1392–1398.
- [11] I. Mosquera-Lois and S. R. Kavanagh, *Matter*, 2021, **4**, 2602–2605.
- [12] A. Kononov, C.-W. Lee, E. P. Shapera and A. Schleife, *Journal of Physics: Condensed Matter*, 2023, **35**, 334002.
- [13] A. G. Squires, L. Ganeshkumar, C. N. Savory, S. R. Kavanagh and D. O. Scanlon, *ACS Energy Letters*, 2024, **9**, 4180–4187.
- [14] W. B. Fowler, M. Stavola, A. Venzie and A. Portoff, *Journal of Applied Physics*, 2024, **135**, 170901.
- [15] T. P. Weiss, O. Ramírez, S. Paetel, W. Witte, J. Nishinaga, T. Feurer and S. Siebentritt, *Physical Review Applied*, 2023, **19**, 024052.
- [16] A. Alkauskas, C. E. Dreyer, J. L. Lyons and C. G. Van de Walle, *Physical Review B*, 2016, **93**, 201304.
- [17] J. B. Varley, H. Peelaers, A. Janotti and C. G. Van De Walle, *Journal of Physics: Condensed Matter*, 2011, **23**, 334212.
- [18] Y. K. Frodason, K. M. Johansen, T. S. Bjørheim, B. G. Svensson and A. Alkauskas, *Physical Review B*, 2017, **95**, 094105.
- [19] Y. K. Frodason, C. Zimmermann, E. F. Verhoeven, P. M. Weiser, L. Vines and J. B. Varley, *Physical Review Materials*, 2021, **5**, 025402.
- [20] I. Mosquera-Lois, S. R. Kavanagh, A. M. Ganose and A. Walsh, *npj Computational Materials*, 2024, **10**, 1–9.
- [21] D. V. Lang and R. A. Logan, *Physical Review Letters*, 1977, **39**, 635–639.
- [22] D. J. Chadi and K. J. Chang, *Physical Review B*, 1989, **39**, 10063–10074.
- [23] S. R. Kavanagh, D. O. Scanlon, A. Walsh and C. Freysoldt, *Faraday Discussions*, 2022, **239**, 339–356.
- [24] B. Dou, S. Falletta, J. Neugebauer, C. Freysoldt, X. Zhang and S.-H. Wei, *Physical Review Applied*, 2023, **19**, 054054.
- [25] J. Cen, B. Zhu, S. R. Kavanagh, A. G. Squires and D. O. Scanlon, *Journal of Materials Chemistry A*, 2023, **11**, 13353–13370.
- [26] A. B. Kehoe, D. O. Scanlon and G. W. Watson, *Chemistry of Materials*, 2011, **23**, 4464–4468.
- [27] X. Wang, S. R. Kavanagh, D. O. Scanlon and A. Walsh, *Physical Review B*, 2023, **108**, 134102.
- [28] S. Lany and A. Zunger, *Physical Review Letters*, 2004, **93**, 156404.
- [29] A. Portoff, M. Stavola, W. B. Fowler, S. J. Pearton and E. R. Glaser, *Applied Physics Letters*, 2023, **122**, 062101.
- [30] Y. Lei and G. Wang, *Scripta Materialia*, 2015, **101**, 20–23.
- [31] P. Mazzolini, J. B. Varley, A. Parisini, A. Sacchi, M. Pavesi, A. Bosio, M. Bosi, L. Seravalli, B. M. Janzen, M. N. Marggraf, N. Bernhardt, M. R. Wagner, A. Ardenghi, O. Bierwagen, A. Falkenstein, J. Kler, R. A. De Souza, M. Martin, F. Mezzadri, C. Borelli and R. Fornari, *Materials Today Physics*, 2024, **45**, 101463.
- [32] H. Okumura and J. B. Varley, *Japanese Journal of Applied Physics*, 2024, **63**, 075502.
- [33] Y. K. Frodason, J. B. Varley, K. M. H. Johansen, L. Vines and C. G. Van de Walle, *Physical Review B*, 2023, **107**, 024109.

- [34] A. Karjalainen, V. Prozheeva, K. Simula, I. Makkonen, V. Callewaert, J. B. Varley and F. Tuomisto, *Physical Review B*, 2020, **102**, 195207.
- [35] A. Karjalainen, I. Makkonen, J. Etula, K. Goto, H. Murakami, Y. Kumagai and F. Tuomisto, *Applied Physics Letters*, 2021, **118**, 072104.
- [36] D. Skachkov, W. R. L. Lambrecht, H. J. von Bardeleben, U. Gerstmann, Q. D. Ho and P. Deák, *Journal of Applied Physics*, 2019, **125**, 185701.
- [37] H. J. von Bardeleben, S. Zhou, U. Gerstmann, D. Skachkov, W. R. L. Lambrecht, Q. D. Ho and P. Deák, *APL Materials*, 2019, **7**, 022521.
- [38] J. M. Johnson, Z. Chen, J. B. Varley, C. M. Jackson, E. Farzana, Z. Zhang, A. R. Arehart, H.-L. Huang, A. Genc, S. A. Ringel, C. G. Van de Walle, D. A. Muller and J. Hwang, *Physical Review X*, 2019, **9**, 041027.
- [39] Y. Qin, M. Stavola, W. B. Fowler, P. Weiser and S. J. Pearton, *ECS Journal of Solid State Science and Technology*, 2019, **8**, Q3103.
- [40] M. Stavola, W. B. Fowler, A. Portoff, A. Venzie, E. R. Glaser and S. J. Pearton, *Journal of Applied Physics*, 2024, **135**, 101101.
- [41] P. Weiser, M. Stavola, W. B. Fowler, Y. Qin and S. Pearton, *Applied Physics Letters*, 2018, **112**, 232104.
- [42] I. Mosquera-Lois, S. R. Kavanagh, A. Walsh and D. O. Scanlon, *Journal of Open Source Software*, 2022, **7**, 4817.
- [43] M. Huang, Z. Zheng, Z. Dai, X. Guo, S. Wang, L. Jiang, J. Wei and S. Chen, *Journal of Semiconductors*, 2022, **43**, 042101.
- [44] A. J. Morris, C. J. Pickard and R. J. Needs, *Physical Review B*, 2008, **78**, 184102.
- [45] M. Arrigoni and G. K. H. Madsen, *npj Computational Materials*, 2021, **7**, 1–13.
- [46] Y. Kumagai, N. Tsunoda, A. Takahashi and F. Oba, *Physical Review Materials*, 2021, **5**, 123803.
- [47] K. Li, J. Willis, S. R. Kavanagh and D. O. Scanlon, *Chemistry of Materials*, 2024, **36**, 2907–2916.
- [48] C. Lee, M. A. Scarpulla and E. Ertekin, *Physical Review Materials*, 2024, **8**, 054603.
- [49] S. R. Kavanagh, A. G. Squires, A. Nicolson, I. Mosquera-Lois, A. M. Ganose, B. Zhu, K. Brlec, A. Walsh and D. O. Scanlon, *Journal of Open Source Software*, 2024, **9**, 6433.
- [50] A. Nicolson, S. R. Kavanagh, C. N. Savory, G. W. Watson and D. O. Scanlon, *Journal of Materials Chemistry A*, 2023, **11**, 14833–14839.
- [51] X. Wang, S. R. Kavanagh, D. O. Scanlon and A. Walsh, *Joule*, 2024, **8**, 2105–2122.
- [52] A. Y. Toukmaji and J. A. Board, *Computer Physics Communications*, 1996, **95**, 73–92.
- [53] S. P. Ong, W. D. Richards, A. Jain, G. Hautier, M. Kocher, S. Cholia, D. Gunter, V. L. Chevrier, K. A. Persson and G. Ceder, *Computational Materials Science*, 2013, **68**, 314–319.
- [54] A. Zhang, H. Li, H. Xu, B. Dou, G. Zhang and W. Wang, *Physical Review Applied*, 2024, **22**, 044047.
- [55] Z. Yuan and G. Hautier, *Applied Physics Letters*, 2024, **124**, 232101.
- [56] B. E. Murdock, J. Cen, A. G. Squires, S. R. Kavanagh, D. O. Scanlon, L. Zhang and N. Tapia-Ruiz, *Advanced Materials*, 2024, **36**, 2400343.
- [57] K. Hoang and M. D. Johannes, *Journal of Materials Chemistry A*, 2014, **2**, 5224–5235.
- [58] Z. Tan, J. Zhang, Y.-C. Chen, J.-P. Chou and Y.-K. Peng, *The Journal of Physical Chemistry Letters*, 2020, **11**, 5390–5396.
- [59] X. Zhang, L. Zhu, Q. Hou, J. Guan, Y. Lu, T. W. Keal, J. Buckeridge, C. R. A. Catlow and A. A. Sokol, *Chemistry of Materials*, 2023, **35**, 207–227.
- [60] T. Grasser, B. Kaczer, W. Goes, T. Aichinger, P. Hehenberger and M. Nelhiebel, 2009 IEEE International Reliability Physics Symposium, 2009, pp. 33–44.

- [61] N. Kuganathan, P. Iyngaran, R. Vovk and A. Chroneos, *Scientific Reports*, 2019, **9**, 4394.
- [62] H. S. Magar, A. M. Mansour and A. B. A. Hammad, *Scientific Reports*, 2024, **14**, 1849.
- [63] B. G. Mullens, F. P. Marlton, M. Saura-Múzquiz, P. A. Chater and B. J. Kennedy, *Inorganic Chemistry*, 2024, **63**, 10386–10396.
- [64] S. Sathasivam, B. A. D. Williamson, A. Kafizas, S. A. Althabaiti, A. Y. Obaid, S. N. Basahel, D. O. Scanlon, C. J. Carmalt and I. P. Parkin, *The Journal of Physical Chemistry C*, 2017, **121**, 202–210.
- [65] C. Han and T. Wang, *Chemical Science*, 2024, **15**, 14371–14378.
- [66] Y. Zhao, C. Deng, D. Tang, L. Ding, Y. Zhang, H. Sheng, H. Ji, W. Song, W. Ma, C. Chen and J. Zhao, *Nature Catalysis*, 2021, **4**, 684–691.
- [67] A. Banerjee, E. F. Holby, A. A. Kohnert, S. Srivastava, M. Asta and B. P. Uberuaga, *Electronic Structure*, 2023, **5**, 024007.
- [68] B. D. Boruah, B. Wen and M. De Volder, *Nano Letters*, 2021, **21**, 3527–3532.
- [69] S. Sucharitakul, G. Ye, W. R. L. Lambrecht, C. Bhandari, A. Gross, R. He, H. Poelman and X. P. A. Gao, *ACS Applied Materials & Interfaces*, 2017, **9**, 23949–23956.
- [70] J. Vinckevičiūtė, M. D. Radin, N. V. Faenza, G. G. Amatucci and A. V. d. Ven, *Journal of Materials Chemistry A*, 2019, **7**, 11996–12007.
- [71] A. R. Genreith-Schriever, C. S. Coates, K. Märker, I. D. Seymour, E. N. Bassegy and C. P. Grey, *Chemistry of Materials*, 2024, **36**, 4226–4239.
- [72] I. Batatia, P. Benner, Y. Chiang, A. M. Elena, D. P. Kovács, J. Riebesell, X. R. Advincula, M. Asta, M. Avaylon, W. J. Baldwin, F. Berger, N. Bernstein, A. Bhowmik, S. M. Blau, V. Cărare, J. P. Darby, S. De, F. D. Pia, V. L. Deringer, R. Elijošius, Z. El-Machachi, F. Falcioni, E. Fako, A. C. Ferrari, A. Genreith-Schriever, J. George, R. E. A. Goodall, C. P. Grey, P. Grigorev, S. Han, W. Handley, H. H. Heenen, K. Hermansson, C. Holm, J. Jaafar, S. Hofmann, K. S. Jakob, H. Jung, V. Kapil, A. D. Kaplan, N. Karimitari, J. R. Kermode, N. Kroupa, J. Kullgren, M. C. Kuner, D. Kuryla, G. Liepuoniute, J. T. Margraf, I.-B. Magdău, A. Michaelides, J. H. Moore, A. A. Naik, S. P. Niblett, S. W. Norwood, N. O’Neill, C. Ortner, K. A. Persson, K. Reuter, A. S. Rosen, L. L. Schaaf, C. Schran, B. X. Shi, E. Sivonxay, T. K. Stenczel, V. Svahn, C. Sutton, T. D. Swinburne, J. Tilly, C. v. d. Oord, E. Varga-Umbrich, T. Vegge, M. Vondrák, Y. Wang, W. C. Witt, F. Zills and G. Csányi, *A foundation model for atomistic materials chemistry*, 2024, <http://arxiv.org/abs/2401.00096>, arXiv:2401.00096 [physics].
- [73] J. Riebesell, R. E. A. Goodall, P. Benner, Y. Chiang, B. Deng, G. Ceder, M. Asta, A. A. Lee, A. Jain and K. A. Persson, *Matbench Discovery – A framework to evaluate machine learning crystal stability predictions*, 2024, <http://arxiv.org/abs/2308.14920>, arXiv:2308.14920 [cond-mat].
- [74] B. Deng, P. Zhong, K. Jun, J. Riebesell, K. Han, C. J. Bartel and G. Ceder, *Nature Machine Intelligence*, 2023, **5**, 1031–1041.
- [75] I. Batatia, D. P. Kovács, G. N. C. Simm, C. Ortner and G. Csányi, *MACE: Higher Order Equivariant Message Passing Neural Networks for Fast and Accurate Force Fields*, 2023, <http://arxiv.org/abs/2206.07697>, arXiv:2206.07697 [cond-mat, physics:physics, stat].
- [76] A. Jain, S. P. Ong, G. Hautier, W. Chen, W. D. Richards, S. Dacek, S. Cholia, D. Gunter, D. Skinner, G. Ceder and K. a. Persson, *APL Materials*, 2013, **1**, 011002.
- [77] A. H. Larsen, J. J. Mortensen, J. Blomqvist, I. E. Castelli, R. Christensen, M. Du\lak, J. Friis, M. N. Groves, B. Hammer, C. Hargus, E. D. Hermes, P. C. Jennings, P. B. Jensen, J. Kermode, J. R. Kitchin, E. L. Kolsbjerg, J. Kubal, K. Kaasbjerg, S. Lysgaard, J. B. Maronsson, T. Maxson, T. Olsen, L. Pastewka, A. Peterson, C. Rostgaard, J. Schiøtz, O. Schütt, M. Strange, K. S. Thygesen, T. Vegge, L. Vilhelmsen, M. Walter, Z. Zeng and K. W. Jacobsen, *Journal of Physics: Condensed Matter*, 2017, **29**, 273002.
- [78] S. Kim, S. N. Hood and A. Walsh, *Physical Review B*, 2019, **100**, 041202.

- [79] X. Wang, S. R. Kavanagh and A. Walsh, *ACS Energy Letters*, 2024, 161–167.
- [80] D. Krasikov and I. Sankin, *Journal of Materials Chemistry A*, 2017, **5**, 3503–3513.
- [81] L. Razinkovas, M. Maciaszek, F. Reinhard, M. W. Doherty and A. Alkauskas, *Physical Review B*, 2021, **104**, 235301.
- [82] Y. Xiong, J. Zheng, S. McBride, X. Zhang, S. M. Griffin and G. Hautier, *Journal of the American Chemical Society*, 2024, **146**, 30046–30056.
- [83] G. Kresse and J. Hafner, *Physical Review B*, 1993, **47**, 558–561.
- [84] G. Kresse and J. Furthmüller, *Computational Materials Science*, 1996, **6**, 15–50.
- [85] G. Kresse and J. Furthmüller, *Physical Review B - Condensed Matter and Materials Physics*, 1996, **54**, 11169–11186.
- [86] G. Kresse and J. Hafner, *Physical Review B*, 1994, **49**, 14251–14269.
- [87] G. Kresse and D. Joubert, *Physical Review B*, 1999, **59**, 1758–1775.
- [88] M. Gajdoš, K. Hummer, G. Kresse, J. Furthmüller and F. Bechstedt, *Physical Review B*, 2006, **73**, 045112.
- [89] P. E. Blöchl, *Physical Review B*, 1994, **50**, 17953–17979.
- [90] C. Adamo and V. Barone, *The Journal of Chemical Physics*, 1999, **110**, 6158–6170.
- [91] J. P. Perdew, A. Ruzsinszky, G. I. Csonka, O. A. Vydrov, G. E. Scuseria, L. A. Constantin, X. Zhou and K. Burke, *Physical Review Letters*, 2008, **100**, 136406.
- [92] J. P. Perdew, K. Burke and M. Ernzerhof, *Physical Review Letters*, 1996, **77**, 3865–3868.
- [93] C. J. Krajewska, S. R. Kavanagh, L. Zhang, D. J. Kubicki, K. Dey, K. Gałkowski, C. P. Grey, S. D. Stranks, A. Walsh, D. O. Scanlon and R. G. Palgrave, *Chemical Science*, 2021, **12**, 14686–14699.
- [94] S. Lany and A. Zunger, *Physical Review B*, 2005, **72**, 035215.
- [95] W. D. Neilson, J. Rizk, M. W. D. Cooper and D. A. Andersson, *The Journal of Physical Chemistry C*, 2024.
- [96] *Andrew-S-Rosen/periodic_trends: Python script to plot periodic trends as a heat map over the periodic table of elements*, https://github.com/Andrew-S-Rosen/periodic_trends.
- [97] M. O’Keefe and N. E. Brese, *Journal of the American Chemical Society*, 1991, **113**, 3226–3229.

Supplementary Material: Split Vacancies with Foundation Models & Electrostatics

S1. ShakeNBreak applied to V_{Ga} in $\alpha\text{-Ga}_2\text{O}_3$

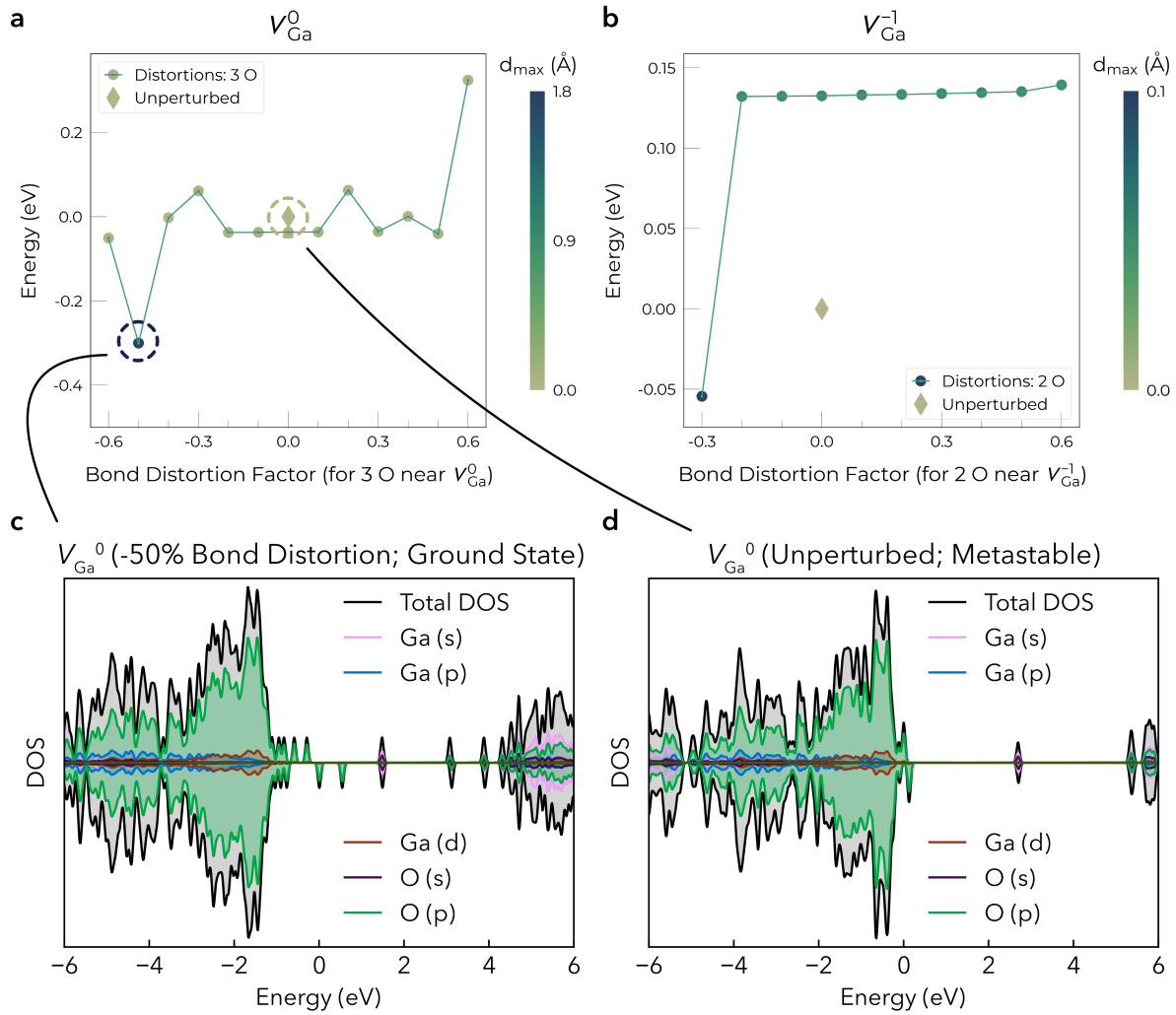


Figure S1. ShakeNBreak⁴² structure searching for V_{Ga} defects in $\alpha\text{-Ga}_2\text{O}_3$ ($R\bar{3}c$). **a,b** Relative energy versus initial bond distortion factor for trial geometries generated by ShakeNBreak, relaxed using PBEsol semi-local DFT, for (a) V_{Ga}^0 and (b) V_{Ga}^{-1} . **c,d** Electronic density of states (DOS) for the (c) ground-state and (d) unperturbed metastable V_{Ga}^0 structures.

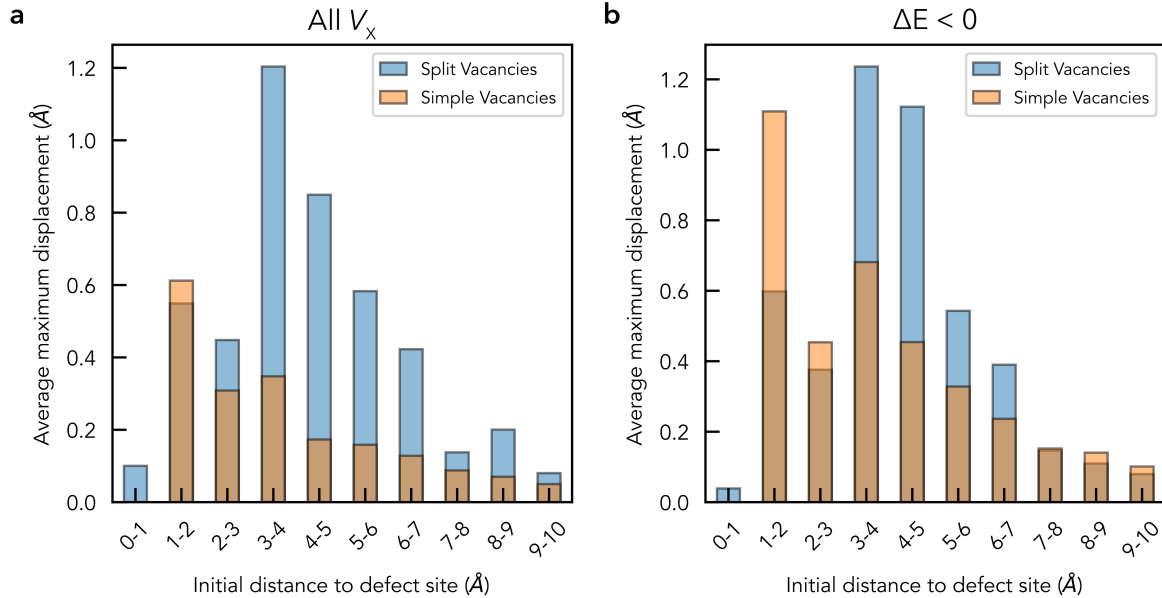


Figure S2. Maximum displacement of atoms in relaxed defect structures, relative to their bulk atomic positions, as a function of initial distance to the defect site, averaged over several thousand defect supercell relaxations for cation vacancies in metal oxides.⁴⁶ Results are plotted separately for relaxations which yielded split vacancy configurations (as classified using the `doped`⁴⁹ site-matching algorithm; see text), vs simple vacancies. Average maximum displacements are shown for all cation vacancy relaxations in (a), while only those for relaxations yielding energy-lowering reconstructions (relative to an unperturbed single vacancy; $\Delta E < 0$) are shown in (b).

S2. Split Vacancy Classification

In order to classify relaxed defect geometries as split vacancies, simple vacancies or ‘non-trivial’ vacancies,⁴⁶ a simple geometric algorithm was employed using the efficient site-matching and structural analysis functions in `doped`,⁴⁹ similar to that employed by Kumagai *et al.*⁴⁶ Specifically, split vacancy geometries were characterised as those where 2 sites from the bulk structure cannot be mapped to any site in the defect structure, and 1 site in the defect structure cannot be mapped to any bulk site, within a chosen distance tolerance (as a fraction of the bulk bond length) – corresponding to the two vacancy and one interstitial sites respectively in the $2V_x + X_i$ definition of a split vacancy geometry (as discussed in the main text). A simple vacancy corresponds to cases where 1 site from the bulk structure cannot be matched to the defect structure while all relaxed defect sites can be matched to bulk sites, and ‘non-trivial’ vacancies are all other cases. In this work, a distance tolerance of 50% of the bulk bond length was used, however this can be tuned by the user within `doped`. The vast majority of relaxed structures in this work are classified as either simple or split vacancies.

S3. Energy Distributions of Candidate Split Vacancies

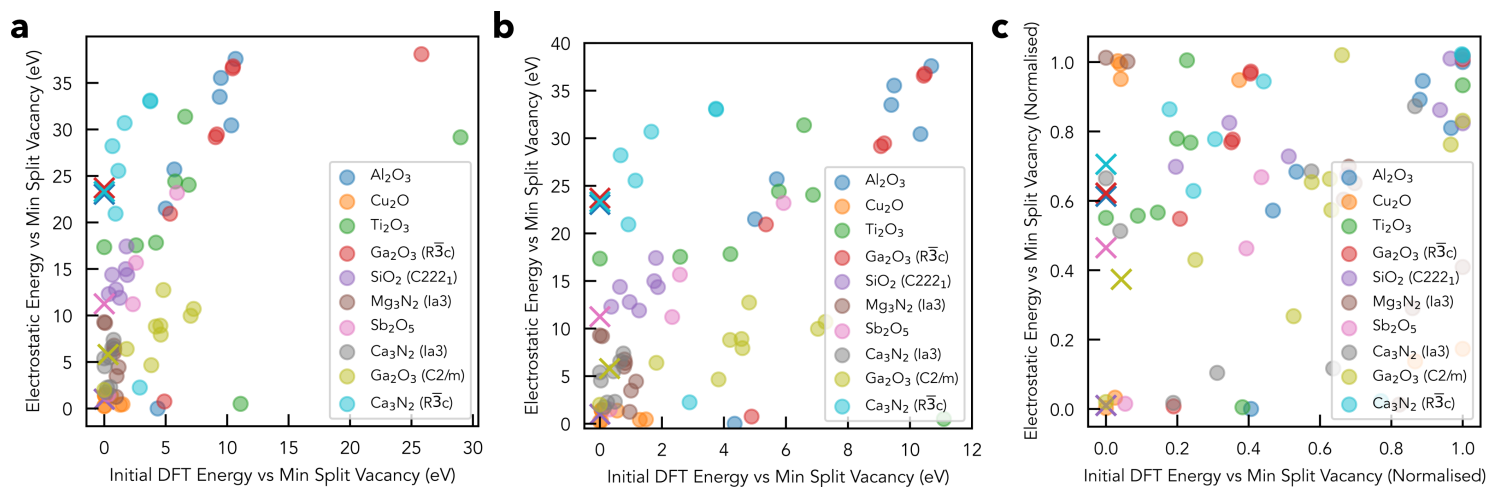


Figure S3. Electrostatic and DFT energies of initial (un-relaxed) candidate split vacancy configurations relative to the minimum energy (un-relaxed) split vacancy structure, across the same initial compound test set as Fig. 2b (V_{Cation} for oxides and V_{Anion} for nitrides). (a) and (b) show the energy distributions over different DFT energy (x -axis) ranges, while (c) shows the energy distributions normalised by the energy range for each compound.

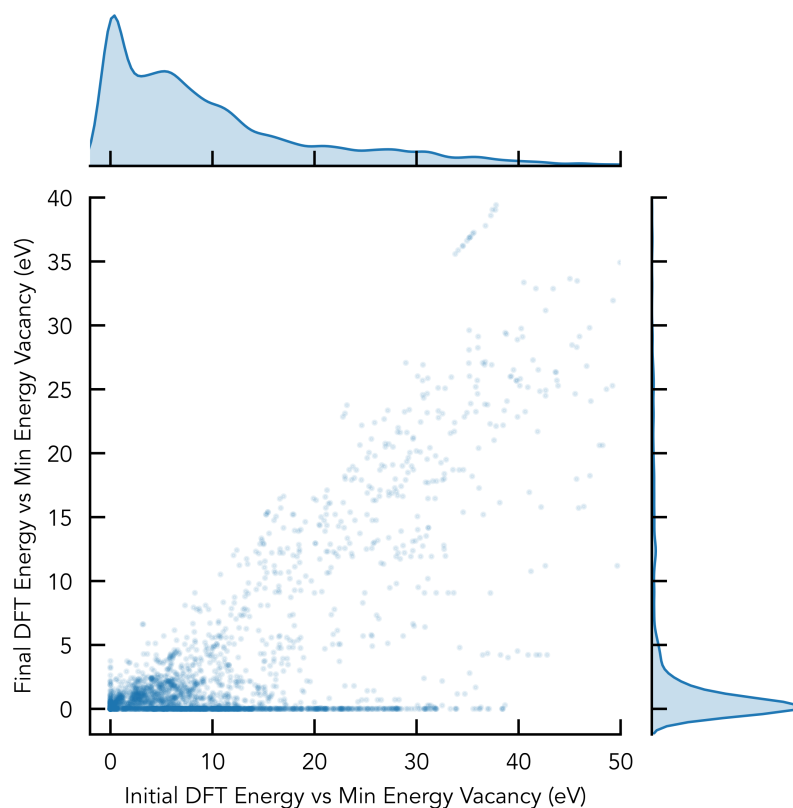


Figure S4. Joint distribution plot of the final vs initial DFT energies of all candidate split vacancies in the full DFT calculated dataset (~ 1000 compounds), relative to the minimum energy candidate split vacancy geometry. ‘Initial’ refers to the fact that these energies are computed for candidate split vacancies before performing geometry relaxation (as in the electrostatic screening step).

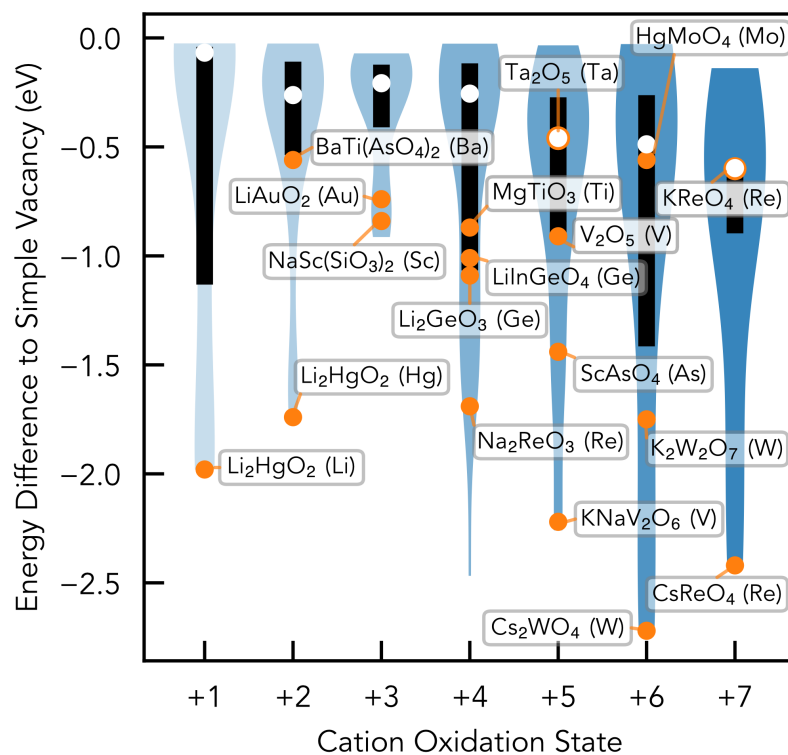


Figure S5. Distribution of energies for all lower energy structures (regardless of split vacancy classification) relative to the lowest energy symmetry-inequivalent point vacancy for different cation oxidation states, for all lower energy vacancies in metal oxides identified in this work ($\Delta E < -0.025$ eV). Some example compounds and the corresponding cation (vacancy) are shown as labelled orange datapoints. White circles and black rectangles denote the median and inter-quartile range respectively.

S4. MACE-mp Foundation Model Geometry Optimisation Tests with ASE⁷⁷

For MACE-mp model size, **small** and **large** were found to perform similarly in terms of predictive accuracy, with **medium** being about 20 % worse. Given the lower runtimes of **small** models (Fig. S9) and similar accuracy, the **small** model was then used for ML-accelerated screening. The recently-released MACE-mp-0b2 model was also tested, giving essentially the same results with a ~10 % speed increase. As mentioned in the Methods section, 32 and 64-bit precision were both tested and showed similar energy accuracies, and so 32-bit (~75 % faster on average) was used for MACE-mp relaxations.

For the MACE-mp geometry optimisation tests shown in Figs. S6 to S9, relaxations were performed for all candidate split vacancy geometries in the metal oxides test set (Fig. 5) which were calculated with DFT, corresponding to ~4,000 supercell relaxations. The GOQN (‘good old quasi Newton’) optimisation algorithm, implemented in the ASE⁷⁷ package was found to be the most accurate and fastest force minimisation algorithm, and so was used for MACE-mp geometry optimisations in the Materials Project⁷⁶ screening. The Gaussian Process Minimiser (GPMIn) algorithm was also trialled, however the high memory demand due to the large supercell sizes caused relaxations to crash.

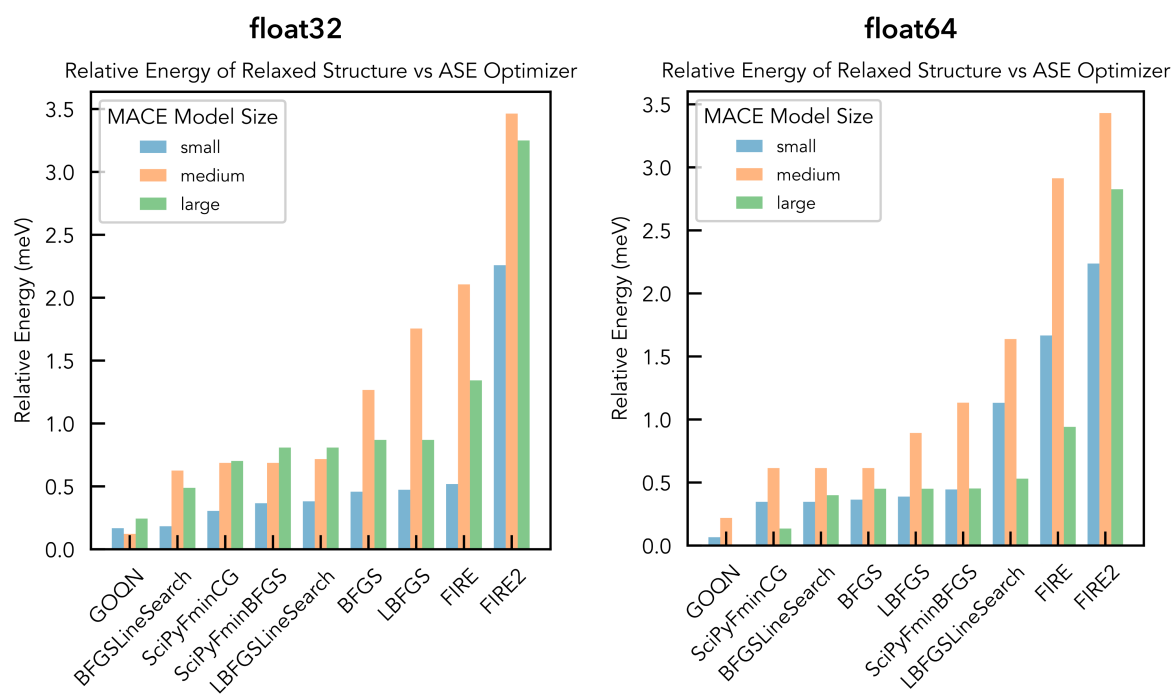


Figure S6. Mean final energies of all MACE-mp geometry optimisations, relative to the lowest energy found for the same input geometry, model size and precision (i.e. out of all optimisation algorithms), as a function of force minimisation algorithm and model size. Results for 32 and 64-bit precisions shown on the left and right respectively.

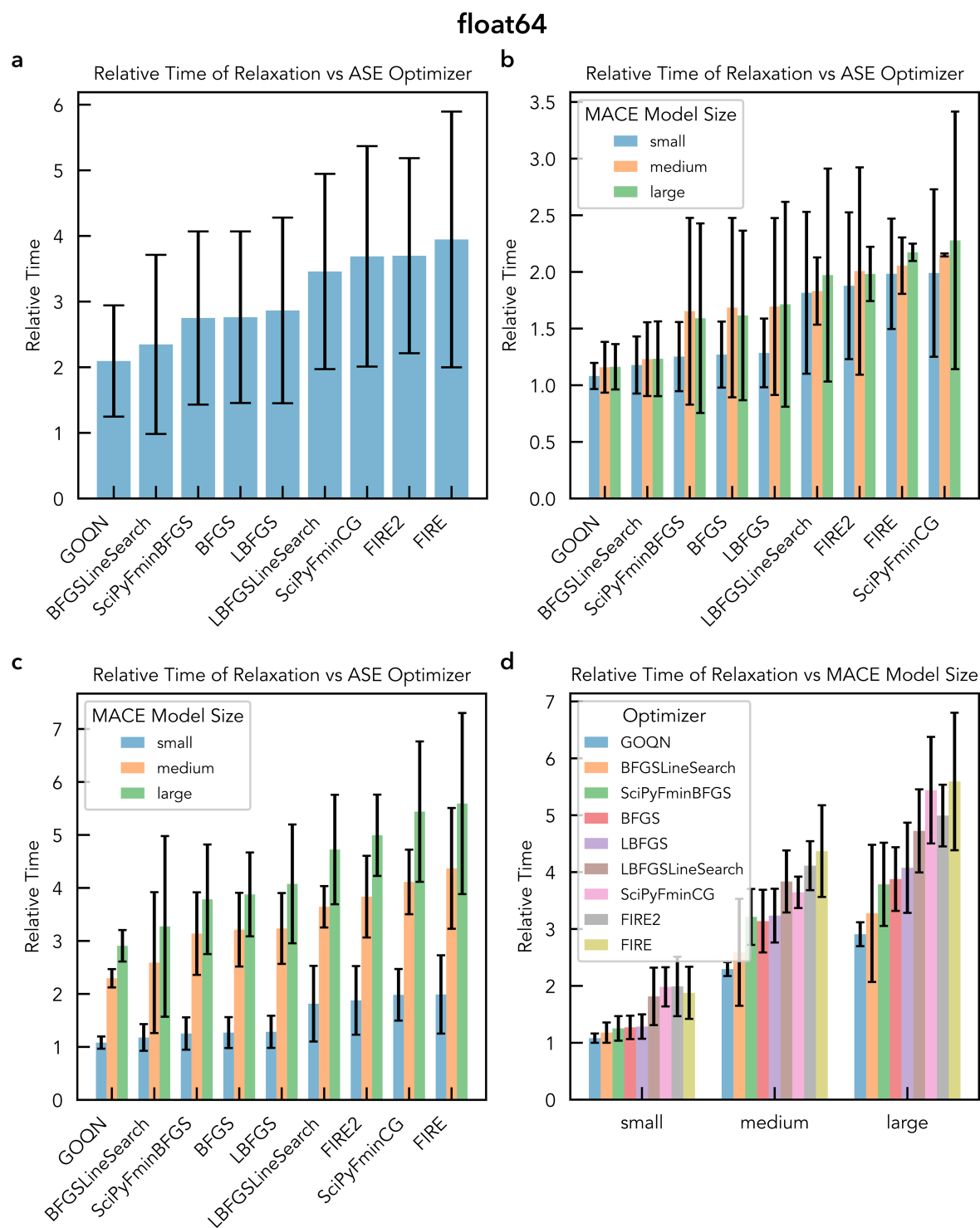


Figure S7. Mean relative runtimes of all MACE-mp geometry optimisations with 64-bit precision, as a function of optimisation algorithm (a), optimisation algorithm and model size (normalised within each model size)(b), optimisation algorithm and model size (normalised to the **small** runtimes)(c), and grouped by model size (again normalised to the **small** runtimes)(d).

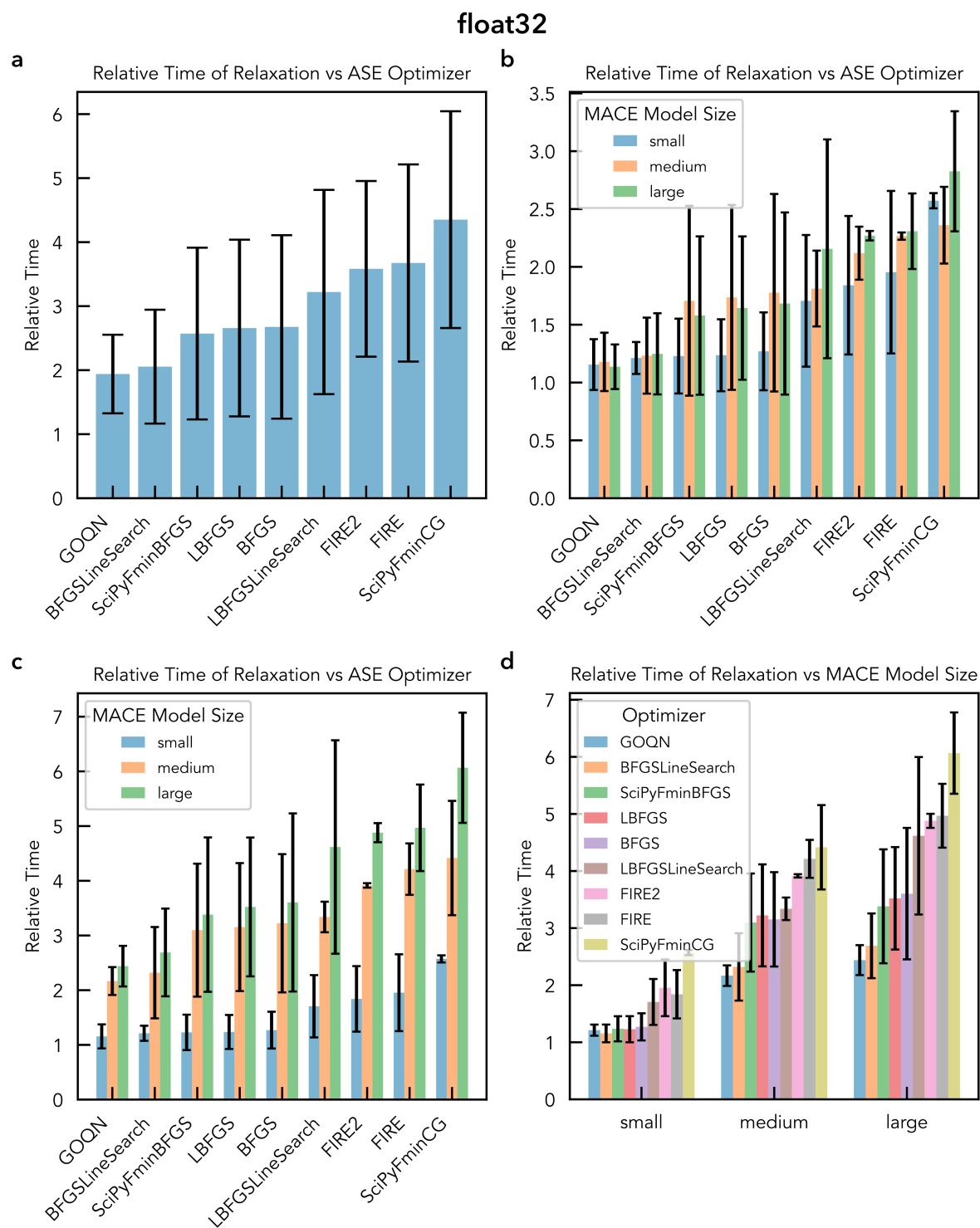


Figure S8. Mean relative runtimes of all MACE-mp geometry optimisations with 32-bit precision, as a function of optimisation algorithm (a), optimisation algorithm and model size (normalised within each model size)(b), optimisation algorithm and model size (normalised to the **small** runtimes)(c), and grouped by model size (again normalised to the **small** runtimes)(d).

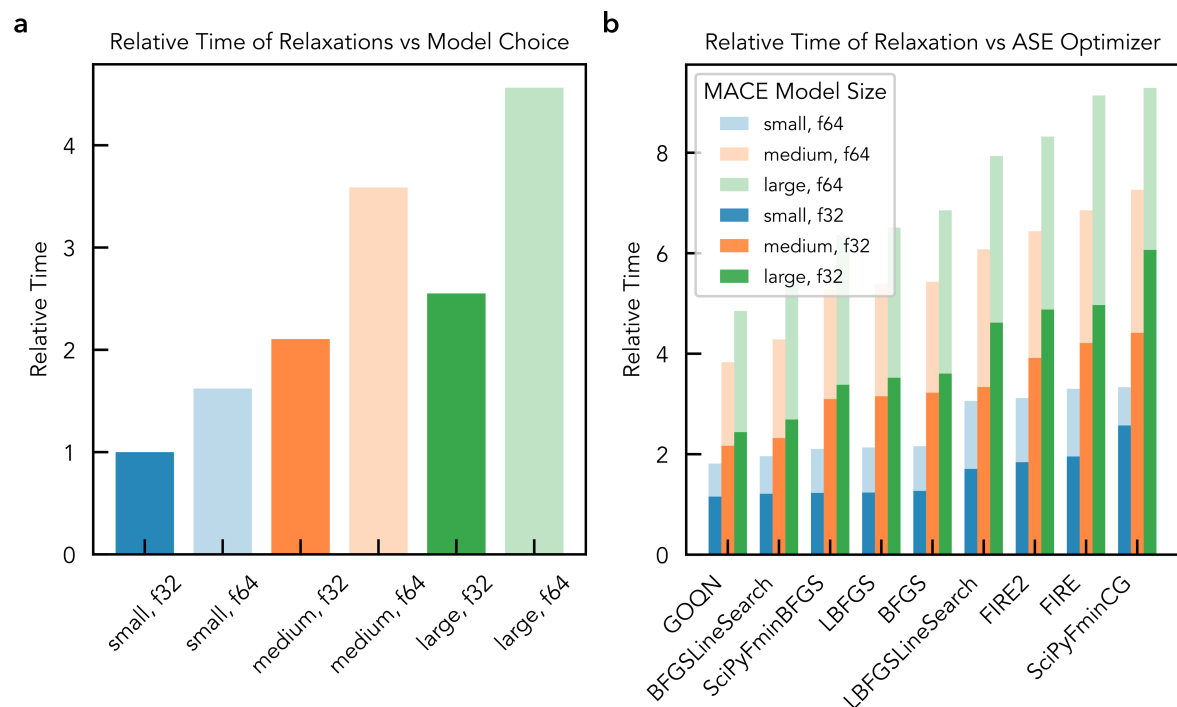


Figure S9. Mean relative runtimes of all MACE-mp geometry optimisations as a function of model size and float precision, averaged over all force minimisation algorithms (a), and separated by optimisation algorithm (b).

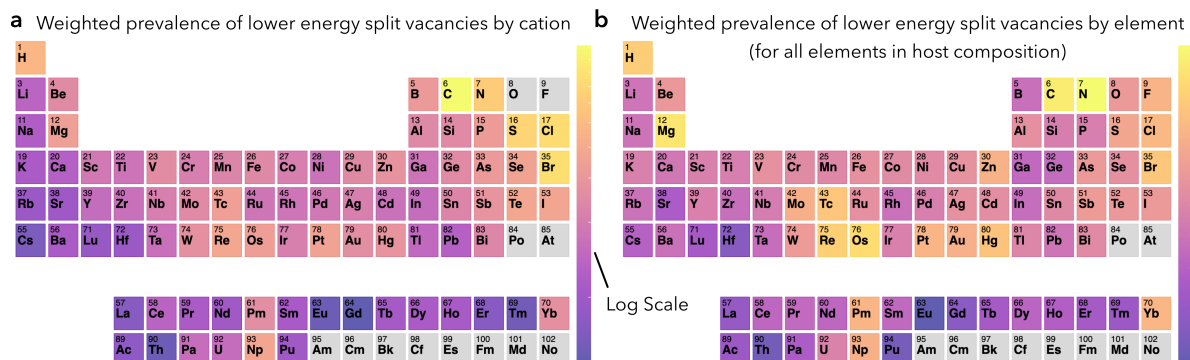


Figure S10. Heatmap plots of the normalised prevalence of lower energy split vacancy states predicted by the ML-accelerated screening of the MP database, for (a) the cation vacancy element and (b) all elements in the corresponding host compound, now weighted by the magnitude of the energy lowering and using a logarithmic scale for the colourbar. Values are normalised by the total prevalence of each element within the dataset.

S5. Identified Metastable States

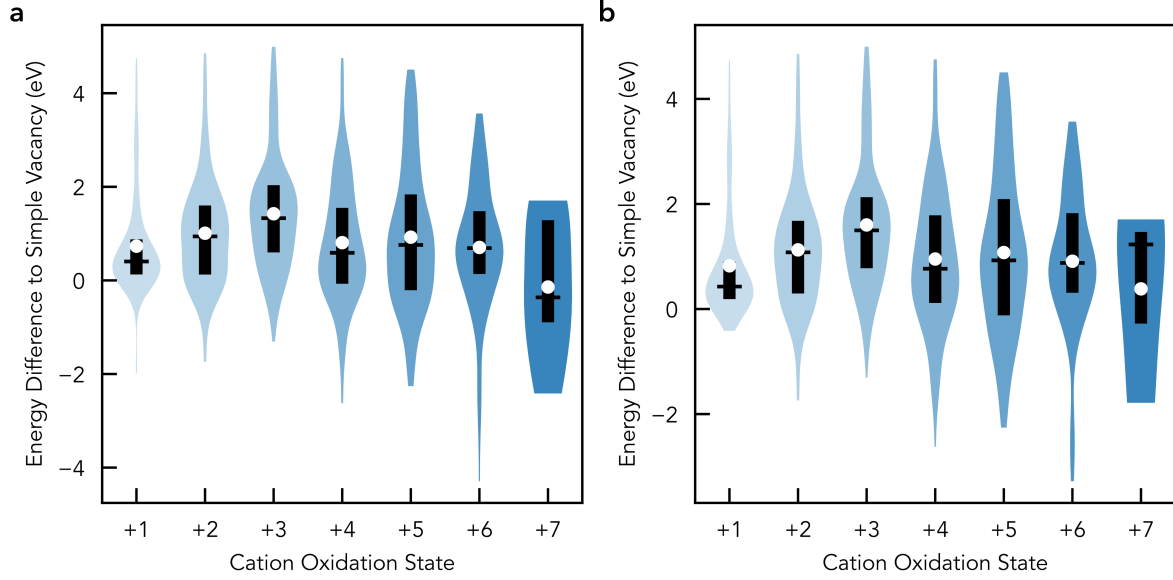


Figure S11. (a) Energy distribution of all distinct metastable states relative to the lowest energy symmetry-inequivalent point vacancy for different cation oxidation states, for all metal oxides calculated in this work. Distinct metastable states are classified as those which (i) relax to a split vacancy geometry (determined by the `doped`⁴⁹ classification algorithm), with no corresponding symmetry-inequivalent point vacancy spontaneously relaxing to a split vacancy, or have a difference in energy >50 meV to any corresponding symmetry-inequivalent point vacancy, and (ii) are different in energy by >25 meV to all other metastable states for that vacancy. Subfigure (b) shows the distributions when *only* split vacancy geometries are included. White circles, black dashes and rectangles denote the mean, median and inter-quartile range respectively.

Table S1: Energies of all distinct metastable states relative to the lowest energy symmetry-inequivalent point vacancy (ΔE), with $\Delta E < 0.5$ eV, for all metal oxides calculated in this work. Distinct metastable states are classified as those which (i) relax to a split vacancy geometry, with no corresponding symmetry-inequivalent point vacancy spontaneously relaxing to a split vacancy, or have a difference in energy >50 meV to any corresponding symmetry-inequivalent point vacancy, and (ii) are different in energy by >25 meV to all other metastable states for that vacancy.

Formula	Cation	Space Group	Energy (eV)	Split Vacancy
Ba ₃ (AsO ₄) ₂	As	R $\bar{3}m$	-1.9	True
Ba ₃ (AsO ₄) ₂	As	R $\bar{3}m$	-0.64	False
LaAsO ₄	As	I4 ₁ /amd	-0.83	True
HfSiO ₄	Si	I4 ₁ /amd	-0.42	True
Ba ₃ V ₂ O ₈	V	R $\bar{3}m$	-1.13	True
Ba ₃ V ₂ O ₈	V	R $\bar{3}m$	-0.54	False
LaVO ₄	V	I4 ₁ /amd	-0.17	True
Na ₂ WO ₄	W	Fd $\bar{3}m$	-3.28	True
Na ₂ WO ₄	W	Fd $\bar{3}m$	-4.29	False
KSbWO ₆	Sb	Ima2	-0.05	False
SrGa ₄ O ₇	Ga	C2/c	-0.14	False
KY(WO ₄) ₂	W	C2/c	-0.98	False
KY(WO ₄) ₂	W	C2/c	0.2	True
Na ₃ SbO ₃	Sb	I $\bar{4}3m$	0.07	False
Rb ₃ YV ₂ O ₈	Rb	P $\bar{3}m1$	-0.33	False

Table S1: Energies of all distinct metastable states relative to the lowest energy symmetry-inequivalent point vacancy (ΔE), with $\Delta E < 0.5$ eV, for all metal oxides calculated in this work. Distinct metastable states are classified as those which (i) relax to a split vacancy geometry, with no corresponding symmetry-inequivalent point vacancy spontaneously relaxing to a split vacancy, or have a difference in energy >50 meV to any corresponding symmetry-inequivalent point vacancy, and (ii) are different in energy by >25 meV to all other metastable states for that vacancy.

Formula	Cation	Space Group	Energy (eV)	Split Vacancy
V ₂ Pb ₃ O ₈	V	P2 ₁ /c	-0.32	False
Sr ₂ MgGe ₂ O ₇	Ge	P4 ₂ 1m	-0.6	False
BiAsO ₄	As	P2 ₁ /c	-0.33	False
HgMoO ₄	Mo	C2/c	0.28	False
HgMoO ₄	Mo	C2/c	-0.56	False
Cs ₆ Ge ₂ O ₇	Cs	P2 ₁ /c	0.01	True
CaIn ₂ O ₄	Ca	Fd3m	-0.28	True
CsBi(MoO ₄) ₂	Mo	Pccm	-2.69	True
K ₃ ScV ₂ O ₈	K	P3m1	-0.42	False
Mg ₄ Nb ₂ O ₉	Nb	P3c1	-1.25	True
MgZn ₂ (AsO ₄) ₂	As	P2 ₁ /c	0.24	False
Mg ₄ Ta ₂ O ₉	Ta	P3c1	-1.83	True
Na ₃ BiO ₃	Bi	I43m	-0.34	False
Sb ₂ O ₅	Sb	C2/c	-1.68	True
Hg ₂ WO ₄	W	C2/c	-0.66	False
BaGa ₄ O ₇	Ga	C2/c	-0.18	True
CsY(WO ₄) ₂	W	C2/c	-0.81	False
Ag ₂ BiO ₃	Ag	Pnn2	0.14	True
SrAl ₄ O ₇	Al	C2/c	-0.21	False
Na ₂ MoO ₄	Mo	Fd3m	-2.18	True
Cs ₁₂ Sn ₂ As ₆ O	Cs	P3m1	0.11	False
Cs ₁₂ Sn ₂ As ₆ O	Cs	P3m1	0.01	True
Cs ₃ BiO ₃	Bi	P2 ₁₃	0.4	False
NaBiO ₃	Bi	R3	-0.46	True
Na ₄ SnO ₃	Sn	Cc	0.49	False
Ba ₄ Nb ₂ O ₉	Nb	P6 ₃ /m	-0.25	False
CaCrO ₄	Cr	I4 ₁ /amd	0.41	True
CaCrO ₄	Cr	I4 ₁ /amd	-0.61	False
KTaWO ₆	K	Ima2	-0.05	True
KTaWO ₆	W	Ima2	0.49	True
KNbWO ₆	K	Ima2	-0.06	False
KNbWO ₆	W	Ima2	0.31	True
CsSbO ₂	Sb	C2/c	0.15	False
Cs ₂ Pb ₂ O ₃	Pb	I2 ₁₃	-0.0	True
Cs ₂ Al ₂ As ₂ O ₇	As	Imm2	0.12	True
Cs ₂ Al ₂ As ₂ O ₇	As	Imm2	0.22	True
LiSbO ₃	Sb	Pnna	-0.25	False
KBi(WO ₄) ₂	W	C2/c	-0.61	False
Sr ₄ Ta ₂ O ₉	Ta	P6 ₃ /m	-0.1	False
CdHgO ₂	Hg	C2/m	0.01	True
MgAl ₂ O ₄	Mg	Fd3m	-0.19	True
NaNbO ₃	Nb	R3	-1.82	True
ScTl(MoO ₄) ₂	Tl	P3m1	-0.16	False
Sr ₄ Nb ₂ O ₉	Nb	P6 ₃ /m	-0.21	False
Rb ₁₂ Sn ₂ As ₆ O	Rb	P3m1	0.09	False
Rb ₁₂ Sn ₂ As ₆ O	Rb	P3m1	-0.01	True
Na ₂ ZnGeO ₄	Na	Pc	0.2	True
KSbWO ₆	K	Ima2	-0.0	True
KSbWO ₆	K	Ima2	-0.05	True
LiGaO ₂	Ga	Pna2 ₁	0.15	True
Rb ₂ SnO ₃	Rb	Cmc2 ₁	0.2	True
V ₂ Pb ₃ O ₈	Pb	P2 ₁ /c	0.0	True
V ₂ Pb ₃ O ₈	Pb	P2 ₁ /c	-0.02	True
CuAsPbO ₄	As	P1	0.21	True
Na ₂ ZnSiO ₄	Na	Pc	0.15	True
K ₂ Zr(BO ₃) ₂	K	R3m	0.36	True
TlSbWO ₆	Tl	Ima2	-0.0	True
Cs ₂ HfO ₃	Cs	Cmcm	0.19	True
Tl ₆ Si ₂ O ₇	Tl	P3	0.3	True

Table S1: Energies of all distinct metastable states relative to the lowest energy symmetry-inequivalent point vacancy (ΔE), with $\Delta E < 0.5$ eV, for all metal oxides calculated in this work. Distinct metastable states are classified as those which (i) relax to a split vacancy geometry, with no corresponding symmetry-inequivalent point vacancy spontaneously relaxing to a split vacancy, or have a difference in energy >50 meV to any corresponding symmetry-inequivalent point vacancy, and (ii) are different in energy by >25 meV to all other metastable states for that vacancy.

Formula	Cation	Space Group	Energy (eV)	Split Vacancy
BaLa ₂ O ₄	Ba	Fd $\bar{3}$ m	0.22	True
Rb ₄ PbO ₄	Rb	P $\bar{1}$	-0.09	False
Cs ₂ Li ₂ GeO ₄	Cs	P $\bar{1}$	0.01	True
Ca ₂ Pt ₃ O ₈	Ca	R $\bar{3}$ m	-0.07	True
CaAl ₄ O ₇	Al	C2/c	0.24	True
K ₂ ZrO ₃	K	Pnma	0.31	True
K ₂ LiVO ₄	K	C2/m	0.39	True
CdSnO ₃	Cd	R $\bar{3}$	0.12	True
CdSnO ₃	Sn	R $\bar{3}$	0.18	True
BaZn ₂ Si ₂ O ₇	Ba	Cmcm	-0.13	True
Li ₄ PbO ₄	Li	Cmcm	0.28	True
K ₂ CdO ₂	K	Pbcn	0.0	True
Cs ₂ SnO ₃	Cs	Cmcm	0.14	True
Li ₂ Si ₂ O ₅	Li	Ccc2	0.05	True
Rb ₂ PbO ₃	Rb	Pnma	0.19	True
CaSnO ₃	Ca	R $\bar{3}$	-0.03	True
CaSnO ₃	Sn	R $\bar{3}$	0.4	True
K ₂ Pb ₂ O ₃	Pb	I2 ₁₃	0.13	True
CaAlBO ₄	Ca	Ccc2	-0.0	True
CaAlBO ₄	Al	Ccc2	0.16	True
TaTiWO ₆	Ti	Ima2	0.04	True
K ₂ Al ₂ Sb ₂ O ₇	K	P $\bar{3}$ m1	0.22	True
Cd(GaO ₂) ₂	Cd	Fd $\bar{3}$ m	0.27	True
K ₄ ZrO ₄	K	P $\bar{1}$	-0.06	False
Li ₄ GeO ₄	Ge	Cmcm	-0.71	True
Li ₄ GeO ₄	Ge	Cmcm	-0.12	False
Cu ₂ PbO ₂	Cu	C2/c	0.41	True
CsTiO	Cs	C2/m	0.35	True
Ca(SbO ₃) ₂	Sb	P $\bar{3}$ 1m	-0.31	True
Rb ₂ ZrO ₃	Rb	Cmc2 ₁	0.25	True
Na ₂ Zn ₂ O ₃	Na	P4 ₃₂ 12	0.14	True
Mg ₂ SnO ₄	Mg	Imma	0.04	True
Cs ₂ O	Cs	R $\bar{3}$ m	0.38	True
Cs ₆ Si ₂ O ₇	Cs	P2 ₁ /c	0.1	True
K ₃ Ta ₃ (BO ₆) ₂	Ta	P $\bar{6}$ 2m	-0.36	True
Tl ₃ BO ₃	Tl	P6 ₃ /m	0.49	True
VAg ₃ HgO ₄	Hg	P1	-0.0	True
VAg ₃ HgO ₄	Ag	P1	0.04	True
Na ₁₄ Cd ₂ O ₉	Na	P $\bar{3}$	0.46	True
As ₂ Pb ₃ O ₈	Pb	P2 ₁ /c	0.04	True
As ₂ Pb ₃ O ₈	Pb	P2 ₁ /c	-0.0	True
LiAg ₃ O ₂	Ag	Ibam	0.19	True
RbTaO ₃	Rb	C2/m	0.03	True
LiAgO	Ag	I4/mmm	0.5	True
Ba ₃ Sb ₂ O	Sb	Pbam	0.03	True
NaVO ₃	V	C2/c	-0.48	True
Na ₂ Sb ₄ O ₇	Na	C2/c	0.3	True
LiSbO ₃	Li	Pnna	0.2	True
NaSbO ₃	Sb	R $\bar{3}$	-0.56	True
K ₂ SnO ₃	K	Pnma	-0.0	True
Sr ₄ Ta ₂ O ₉	Sr	P6 ₃ /m	-0.01	True
CdIn ₂ O ₄	Cd	Fd $\bar{3}$ m	0.27	True
Ta ₂ Zn ₃ O ₈	Zn	C2/c	0.04	True
CaGaBO ₄	Ca	Ccc2	-0.03	True
CaGaBO ₄	Ga	Ccc2	0.02	True
K ₂ LiBO ₃	K	C2	0.02	True
K ₂ Sn ₂ O ₃	Sn	I2 ₁₃	0.29	True
Rb ₂ Pb ₂ O ₃	Pb	I2 ₁₃	0.12	True
Nb ₂ SnO ₆	Nb	C2/c	0.45	True

Table S1: Energies of all distinct metastable states relative to the lowest energy symmetry-inequivalent point vacancy (ΔE), with $\Delta E < 0.5$ eV, for all metal oxides calculated in this work. Distinct metastable states are classified as those which (i) relax to a split vacancy geometry, with no corresponding symmetry-inequivalent point vacancy spontaneously relaxing to a split vacancy, or have a difference in energy >50 meV to any corresponding symmetry-inequivalent point vacancy, and (ii) are different in energy by >25 meV to all other metastable states for that vacancy.

Formula	Cation	Space Group	Energy (eV)	Split Vacancy
As ₂ O ₃	As	P2 ₁ /c	0.28	True
Ba(AsO ₃) ₂	Ba	C2/c	-0.91	False
Ba(AsO ₃) ₂	As	C2/c	-0.54	False
BeTiAsO ₄	As	Pna2 ₁	-0.37	False
CsBeAsO ₄	Cs	Pna2 ₁	0.18	False
LaSbO ₄	Sb	P2 ₁ /c	-0.06	False
NaSrBO ₃	Sr	P2 ₁ /c	-0.07	False
AlTi(MoO ₄) ₂	Tl	P3m1	-0.06	False
Sr ₂ ZnGe ₂ O ₇	Ge	P4 ₂ 1m	-0.5	False
Ba ₃ CaNb ₂ O ₉	Ba	P3m1	-0.51	False
Ba ₃ Nb ₂ CdO ₉	Ba	P3m1	-0.45	False
NaLiV ₂ O ₆	V	C2/c	-0.71	True
Ta ₂ Mo ₂ O ₁₁	Ta	R3m	0.27	False
Ba ₃ SrTa ₂ O ₉	Ta	P6 ₃ /m	0.21	False
RbIn(MoO ₄) ₂	Rb	P3m1	-0.21	False
Na ₄ SnO ₄	Sn	P1	-0.12	False
As ₂ Pb ₃ O ₈	As	P2 ₁ /c	-0.19	False
La ₂ CrO ₆	Cr	C2/c	-0.46	False
TiBi ₂ O ₅	Ti	Cmc2 ₁	-0.25	True
BaTi(SiO ₃) ₃	Si	P6c2	0.11	True
BaTi(SiO ₃) ₃	Si	P6c2	-0.07	False
Mg ₂ TiO ₄	Mg	P4 ₁₂₂	0.37	True
Mg ₂ TiO ₄	Mg	P4 ₁₂₂	0.32	True
TiTi ₂ O ₃	Tl	Pnma	0.42	True
TiTi ₂ O ₃	Tl	Pnma	0.04	True
TiTi ₂ O ₃	Tl	Pnma	0.27	True
MgTiO ₃	Mg	R3	0.12	True
MgTiO ₃	Ti	R3	-0.87	True
KLaTiO ₄	K	P4/nmm	-0.09	False
KLaTiO ₄	La	P4/nmm	-0.07	False
TiTi ₂ (GeO ₃) ₃	Ge	P6 ₃ /m	-0.01	True
TiTi ₂ (GeO ₃) ₃	Ge	P6 ₃ /m	-1.53	True
TiTi ₂ (GeO ₃) ₃	Tl	P6 ₃ /m	0.2	False
SrTiO ₃	Sr	I4/mcm	-0.1	False
SrTiO ₃	Sr	I4/mcm	-0.08	False
TiO ₂	Ti	C2/m	0.31	True
TiNb ₆ Tl ₂ O ₁₈	Tl	P3m1	0.13	True
TiNb ₆ Tl ₂ O ₁₈	Tl	P3m1	0.06	True
TiSnO ₃	Ti	R3	0.43	True
TiSnO ₃	Sn	R3	0.45	True
K ₂ TiO ₃	K	Cmcm	0.21	True
Li ₄ TiO ₄	Ti	Cmcm	-1.18	True
LaTiSbO ₆	Sb	P312	0.45	True
Ba ₂ Ti(GeO ₄) ₂	Ba	P4bm	-0.11	False
Ba ₂ Ti(GeO ₄) ₂	Ba	P4bm	-0.26	False
Ba ₂ Ti(GeO ₄) ₂	Ba	P4bm	0.28	False
Ba ₂ Ti(GeO ₄) ₂	Ba	P4bm	0.08	False
Ba ₂ Ti(GeO ₄) ₂	Ba	P4bm	0.39	False
Ba ₂ Ti(GeO ₄) ₂	Ba	P4bm	-0.16	False
Ba ₂ Ti(GeO ₄) ₂	Ba	P4bm	-0.21	False
Ba ₂ Ti(GeO ₄) ₂	Ge	P4bm	0.24	False
Ba ₂ Ti(GeO ₄) ₂	Ge	P4bm	-0.13	False
Ba ₂ Ti(GeO ₄) ₂	Ge	P4bm	0.14	False
Rb ₂ TiO ₃	Rb	Cmce	0.35	True
BaTi(AsO ₄) ₂	Ba	C2/m	-0.55	False
BaTi(AsO ₄) ₂	Ba	C2/m	-0.39	False
BaTi(AsO ₄) ₂	As	C2/m	-1.07	True
BaTi(AsO ₄) ₂	As	C2/m	-0.44	False
Ta ₆ TiTi ₂ O ₁₈	Ta	P3m1	-0.2	False

Table S1: Energies of all distinct metastable states relative to the lowest energy symmetry-inequivalent point vacancy (ΔE), with $\Delta E < 0.5$ eV, for all metal oxides calculated in this work. Distinct metastable states are classified as those which (i) relax to a split vacancy geometry, with no corresponding symmetry-inequivalent point vacancy spontaneously relaxing to a split vacancy, or have a difference in energy >50 meV to any corresponding symmetry-inequivalent point vacancy, and (ii) are different in energy by >25 meV to all other metastable states for that vacancy.

Formula	Cation	Space Group	Energy (eV)	Split Vacancy
Ta ₆ TiTi ₂ O ₁₈	Tl	P $\bar{3}$ m1	0.07	True
Ta ₆ TiTi ₂ O ₁₈	Tl	P $\bar{3}$ m1	0.0	True
Ta ₆ TiTi ₂ O ₁₈	Tl	P $\bar{3}$ m1	-0.02	True
Na ₂ TiGeO ₅	Na	P4/nmm	0.43	True
La ₃ TiGa ₅ O ₁₄	Ga	P321	0.5	True
TiCdO ₃	Cd	R $\bar{3}$	0.3	True
TiCdO ₃	Ti	R $\bar{3}$	0.48	True
Sc ₂ Ti ₂ O ₇	Ti	C2/m	0.09	False
Sc ₂ Ti ₂ O ₇	Ti	C2/m	-0.39	True
Na ₂ TiSiO ₅	Na	P4/nmm	0.43	True
MoPb ₂ O ₅	Mo	C2/m	-0.27	False
MoPb ₂ O ₅	Mo	C2/m	-0.18	False
Sr(AsO ₃) ₂	As	P6 ₃ /mcm	0.03	True
NaCaAsO ₄	As	Pnma	-0.31	True
NaCaAsO ₄	As	Pnma	0.15	False
NaCaAsO ₄	As	Pnma	-0.13	True
NaCaAsO ₄	Na	Pnma	0.45	True
Li ₂ SnO ₃	Li	C2/c	0.19	True
Li ₂ SnO ₃	Li	C2/c	0.22	True
YAsO ₄	As	I4 ₁ /amd	-1.57	True
RbReO ₄	Re	I4 ₁ /a	-0.59	False
K ₃ AlO ₃	K	C2/m	0.15	True
BaGeO ₃	Ge	P2 ₁ $\bar{2}$ ₁ $\bar{2}$ ₁	-0.05	True
Na ₅ NbO ₅	Na	C2/c	-0.0	True
ZrSiO ₄	Si	I4 ₁ /amd	-0.2	True
Rb ₂ MoO ₄	Rb	C2/m	0.35	True
NaBi(MoO ₄) ₂	Mo	I $\bar{4}$	0.46	False
Ba ₂ PbO ₄	Ba	I4/mmm	-0.17	False
Rb ₂ W ₂ O ₇	W	P2 ₁ /c	-0.34	True
Rb ₂ W ₂ O ₇	Rb	P2 ₁ /c	0.09	True
RbBa ₄ Sb ₃ O	Sb	I4/mcm	0.01	True
Cs ₃ TlO ₃	Cs	P2 ₁ /c	0.19	True
As ₂ PbO ₄	As	P2 ₁ /c	0.33	True
As ₂ PbO ₄	As	P2 ₁ /c	-0.01	True
Cs ₂ SrV ₄ O ₁₂	V	P4/mmm	-2.26	True
K ₂ WO ₄	K	C2/m	0.29	True
KNaV ₂ O ₆	V	C2/c	-2.22	False
Au ₂ O ₃	Au	Fdd2	0.4	True
KLa ₂ NbO ₆	K	C2/m	0.25	True
KLa ₂ NbO ₆	Nb	C2/m	-0.18	True
V ₂ O ₅	V	Pmmn	0.16	True
V ₂ O ₅	V	Pmmn	-0.88	True
V ₂ O ₅	V	Pmmn	-0.61	True
V ₂ O ₅	V	Pmmn	-0.38	True
V ₂ O ₅	V	Pmmn	-0.91	True
Mg(GaO ₂) ₂	Ga	Imma	0.44	True
Mg(GaO ₂) ₂	Ga	Imma	-0.0	True
RbBO ₂	Rb	R $\bar{3}$ c	0.34	True
K ₂ MgO ₂	K	Pbcn	0.0	True
Rb ₃ GaO ₃	Rb	C2/m	0.21	True
K ₂ Zn(GeO ₃) ₂	K	C222 ₁	0.49	True
K ₂ Zn(GeO ₃) ₂	K	C222 ₁	0.41	True
K ₂ Zn(GeO ₃) ₂	Ge	C222 ₁	-0.61	False
Li ₂ GeO ₃	Ge	Cmc2 ₁	-1.09	True
NaAg ₃ O ₂	Ag	Ibam	0.22	True
KBO ₂	K	R $\bar{3}$ c	0.37	True
Cs ₂ Li ₃ GaO ₄	Cs	Ibam	0.24	True
BaMoO ₄	Mo	I4 ₁ /a	0.42	True
SrCrO ₄	Cr	P2 ₁ /c	0.13	True

Table S1: Energies of all distinct metastable states relative to the lowest energy symmetry-inequivalent point vacancy (ΔE), with $\Delta E < 0.5$ eV, for all metal oxides calculated in this work. Distinct metastable states are classified as those which (i) relax to a split vacancy geometry, with no corresponding symmetry-inequivalent point vacancy spontaneously relaxing to a split vacancy, or have a difference in energy >50 meV to any corresponding symmetry-inequivalent point vacancy, and (ii) are different in energy by >25 meV to all other metastable states for that vacancy.

Formula	Cation	Space Group	Energy (eV)	Split Vacancy
SrCrO ₄	Cr	P2 ₁ /c	-0.0	True
SrCrO ₄	Cr	P2 ₁ /c	0.23	False
Rb ₂ WO ₄	W	C2/m	0.18	False
Rb ₂ WO ₄	Rb	C2/m	0.33	True
Tl ₃ AsO ₄	Tl	P6 ₃	0.13	True
LiSb ₃ O ₈	Sb	P2 ₁ /c	0.16	True
LiSb ₃ O ₈	Sb	P2 ₁ /c	-0.49	True
LiSb ₃ O ₈	Sb	P2 ₁ /c	-0.36	True
Hg(SbO ₃) ₂	Sb	P $\bar{3}$ 1m	0.26	True
LiSc(WO ₄) ₂	W	C2/c	-0.47	True
LiSc(WO ₄) ₂	W	C2/c	0.38	True
RbSbO ₂	Sb	C2/c	0.28	True
Rb ₂ Sn ₂ O ₃	Sn	R $\bar{3}$ m	-0.12	False
Rb ₂ Sn ₂ O ₃	Rb	R $\bar{3}$ m	-0.07	False
SbAsO ₃	As	P2 ₁ /c	0.28	False
SbAsO ₃	Sb	P2 ₁ /c	0.49	True
CrPb ₂ O ₅	Cr	C2/m	0.03	True
Rb ₃ TlO ₃	Rb	P2 ₁ /c	0.27	True
CsLaO ₂	Cs	P6 ₃ /mmc	0.47	True
LiCuO	Li	I4/mmm	0.47	True
Rb ₂ Li ₃ GaO ₄	Rb	Ibam	0.2	True
NaIn(WO ₄) ₂	W	P2/c	0.43	True
NaIn(WO ₄) ₂	W	P2/c	0.23	True
NaIn(WO ₄) ₂	W	P2/c	-0.26	True
Sb ₂ O ₃	Sb	Pccn	0.32	True
Na ₂ ReO ₃	Re	P6 ₃ /mcm	-1.69	True
Na ₂ ReO ₃	Na	P6 ₃ /mcm	0.46	True
RbLiZn ₂ O ₃	Rb	P4 ₂ /mnm	0.18	True
ScAsO ₄	As	I4 ₁ /amd	-1.44	True
K ₂ ZnO ₂	K	Ibam	-0.0	True
KReO ₄	Re	I4 ₁ /a	-0.14	False
KReO ₄	Re	I4 ₁ /a	-0.6	False
Cs ₂ Sn(GeO ₃) ₃	Ge	P6 ₃ /m	-1.47	True
Cs ₂ Sn(GeO ₃) ₃	Ge	P6 ₃ /m	-2.47	False
Cs ₂ Sn(GeO ₃) ₃	Ge	P6 ₃ /m	-1.55	True
LiAuO ₂	Au	I4 ₁₂₂	-0.74	False
NaAuO ₂	Au	C2/m	0.41	True
Y ₂ Pb ₂ O ₇	Pb	Fd $\bar{3}$ m	-0.43	False
Zn ₂ PtO ₄	Pt	Imma	0.49	True
Zn ₂ PtO ₄	Zn	Imma	-0.38	True
Na ₅ TaO ₅	Na	C2/c	-0.0	True
Rb ₂ MgO ₂	Rb	Ibam	0.0	True
HgAsO ₃	As	P $\bar{3}$ 1m	0.43	True
HgAsO ₃	As	P $\bar{3}$ 1m	-0.17	False
KTa(GeO ₃) ₃	Ge	P $\bar{6}$ c2	0.42	True
KTa(GeO ₃) ₃	Ge	P $\bar{6}$ c2	0.16	True
KTa(GeO ₃) ₃	Ge	P $\bar{6}$ c2	-0.09	False
Cd(SbO ₃) ₂	Sb	P $\bar{3}$ 1m	-0.26	True
GeO ₂	Ge	P3 ₁₂₁	0.13	True
K ₃ GaO ₃	K	C2/m	0.13	True
Rb ₂ Si ₃ SnO ₉	Rb	P6 ₃ /m	0.43	True
Na ₃ AgO ₂	Na	Ibam	0.43	True
NaSc(SiO ₃) ₂	Sc	C2/c	-0.84	False
Ba ₂ Bi ₂ O ₅	Bi	P2 ₁ /c	0.11	False
Ba ₂ Bi ₂ O ₅	Bi	P2 ₁ /c	0.3	False
Ca ₂ Sn ₃ O ₈	Sn	C2/m	0.47	True
Na ₄ As ₂ O ₇	As	C2/c	0.32	True
K ₂ Zn(SiO ₃) ₂	K	C222 ₁	0.37	True
K ₂ Zn(SiO ₃) ₂	K	C222 ₁	0.4	True

Table S1: Energies of all distinct metastable states relative to the lowest energy symmetry-inequivalent point vacancy (ΔE), with $\Delta E < 0.5$ eV, for all metal oxides calculated in this work. Distinct metastable states are classified as those which (i) relax to a split vacancy geometry, with no corresponding symmetry-inequivalent point vacancy spontaneously relaxing to a split vacancy, or have a difference in energy >50 meV to any corresponding symmetry-inequivalent point vacancy, and (ii) are different in energy by >25 meV to all other metastable states for that vacancy.

Formula	Cation	Space Group	Energy (eV)	Split Vacancy
K ₂ Zn(SiO ₃) ₂	Si	C222 ₁	0.12	True
K ₂ Zn(SiO ₃) ₂	Si	C222 ₁	-0.11	True
K ₂ Zn(SiO ₃) ₂	Si	C222 ₁	-0.37	True
TlV ₂ AgO ₆	V	C2/c	0.06	True
TlV ₂ AgO ₆	V	C2/c	-0.4	True
Cs ₃ InO ₃	Cs	P2 ₁ /c	0.11	True
Zr(MoO ₄) ₂	Mo	P $\bar{3}$ m1	-0.21	True
LiTa ₃ O ₈	Ta	C2/c	0.12	False
LiTa ₃ O ₈	Ta	C2/c	-0.28	True
CaMgGeO ₄	Ge	Pnma	0.07	True
KAgO ₂	K	Cmcm	0.41	True
Cs ₃ AlO ₃	Cs	P2 ₁ /c	0.01	True
BaSn(GeO ₃) ₃	Ba	P $\bar{6}$ c2	-0.08	False
BaSn(GeO ₃) ₃	Ge	P $\bar{6}$ c2	-1.44	True
Mg ₃ V ₂ O ₈	V	Cmce	-0.23	True
RbNaCd ₃ O ₄	Rb	Cm	0.4	True
Ga ₂ O ₃	Ga	C2/m	-0.27	True
Ga ₂ O ₃	Ga	C2/m	0.15	True
Ga ₂ O ₃	Ga	C2/m	-0.75	True
KBa ₄ Sb ₃ O	K	I4/mcm	0.49	True
KBa ₄ Sb ₃ O	Sb	I4/mcm	0.07	True
Li ₆ ZnO ₄	Li	P4 ₂ /nmc	0.07	True
Rb ₂ HgO ₂	Rb	I4/mmm	0.45	True
LiInGeO ₄	Li	Pnma	0.28	True
LiInGeO ₄	Ge	Pnma	-1.01	True
CsReO ₄	Re	Pnma	-1.79	True
CsReO ₄	Re	Pnma	-2.42	False
Na ₄ B ₂ O ₅	Na	C2/c	0.36	False
NaCuO ₂	Na	Cmcm	0.32	True
Hg ₂ GeO ₄	Hg	Fddd	0.49	True
NaIn(SiO ₃) ₂	In	C2/c	-0.91	False
LiScSiO ₄	Li	Pnma	0.32	True
LiScSiO ₄	Si	Pnma	0.07	True
VBiO ₄	V	I4 ₁ /amd	-0.0	True
KTaO ₃	K	Pm $\bar{3}$ m	-1.13	False
BaHf(SiO ₃) ₃	Si	P $\bar{6}$ c2	-0.19	True
Li ₂ HgO ₂	Hg	I4/mmm	-0.65	True
Li ₂ HgO ₂	Hg	I4/mmm	-0.96	True
Li ₂ HgO ₂	Hg	I4/mmm	-1.04	True
Li ₂ HgO ₂	Hg	I4/mmm	-1.66	True
Li ₂ HgO ₂	Hg	I4/mmm	0.2	True
Li ₂ HgO ₂	Hg	I4/mmm	-0.35	True
Li ₂ HgO ₂	Hg	I4/mmm	0.1	True
Li ₂ HgO ₂	Hg	I4/mmm	-0.05	True
Li ₂ HgO ₂	Hg	I4/mmm	-1.74	True
Li ₂ HgO ₂	Hg	I4/mmm	0.01	True
Li ₂ HgO ₂	Hg	I4/mmm	-0.53	True
Li ₂ HgO ₂	Hg	I4/mmm	-1.52	True
Li ₂ HgO ₂	Hg	I4/mmm	0.29	True
Li ₂ HgO ₂	Li	I4/mmm	0.32	True
Li ₂ HgO ₂	Li	I4/mmm	-0.42	True
Li ₂ HgO ₂	Li	I4/mmm	-1.98	False
Li ₂ HgO ₂	Li	I4/mmm	-1.95	False
Li ₂ HgO ₂	Li	I4/mmm	-1.82	False
YVO ₄	V	I4 ₁ /amd	-0.77	True
Ge ₃ Sb ₂ O ₉	Ge	P6 ₃ /m	-0.3	False
Ge ₃ Sb ₂ O ₉	Ge	P6 ₃ /m	0.14	False
Ge ₃ Sb ₂ O ₉	Sb	P6 ₃ /m	-0.22	False
Ge ₃ Sb ₂ O ₉	Sb	P6 ₃ /m	-0.02	True

Table S1: Energies of all distinct metastable states relative to the lowest energy symmetry-inequivalent point vacancy (ΔE), with $\Delta E < 0.5$ eV, for all metal oxides calculated in this work. Distinct metastable states are classified as those which (i) relax to a split vacancy geometry, with no corresponding symmetry-inequivalent point vacancy spontaneously relaxing to a split vacancy, or have a difference in energy >50 meV to any corresponding symmetry-inequivalent point vacancy, and (ii) are different in energy by >25 meV to all other metastable states for that vacancy.

Formula	Cation	Space Group	Energy (eV)	Split Vacancy
GePbO ₃	Ge	R $\bar{3}$	-0.47	True
Si ₂ Hg ₆ O ₇	Hg	C2/m	0.42	True
KAuO ₂	K	Cmcm	0.4	True
Ta ₂ O ₅	Ta	Pmmn	-0.08	False
Ta ₂ O ₅	Ta	Pmmn	-0.46	True
LiInSiO ₄	Li	Pnma	0.39	True
LiInSiO ₄	Si	Pnma	-0.15	True
Li ₅ BiO ₅	Li	C2/m	0.09	False
Cs ₃ YO ₃	Cs	P2 ₁ /c	0.15	True
Rb ₃ InO ₃	Rb	P2 ₁ /c	0.18	True
Cs ₂ Zr(SiO ₃) ₃	Cs	P6 ₃ /m	0.49	True
Mg ₂ GeO ₄	Ge	Pnma	-0.03	True
AlSbO ₄	Sb	Cmmm	0.45	True
TlSbO ₃	Sb	P $\bar{3}$ 1c	0.3	True
TlSbO ₃	Sb	P $\bar{3}$ 1c	-0.37	False
TlSbO ₃	Tl	P $\bar{3}$ 1c	-0.06	False
Cd ₂ SiO ₄	Cd	Fddd	0.31	True
Cd ₂ SiO ₄	Cd	Fddd	0.24	True
Na ₆ PbO ₅	Pb	Cmcm	-0.14	False
Na ₆ PbO ₅	Pb	Cmcm	0.07	False
Mg(CuO ₂) ₂	Mg	Pbcm	-0.15	False
Mg(CuO ₂) ₂	Mg	Pbcm	-0.46	False
CsBO ₂	Cs	R $\bar{3}$ c	0.31	True
CdWO ₄	W	P2/c	-0.49	True
CdWO ₄	W	P2/c	-1.42	False
Cd ₃ SiO ₅	Cd	P4/nmm	0.38	True
CaGa ₄ O ₇	Ga	C2/c	0.09	False
MgGeO ₃	Ge	C2/c	-0.89	True
MgGeO ₃	Ge	C2/c	-0.1	True
ScVO ₄	V	I4 ₁ /amd	-0.72	True
ScVO ₄	V	I4 ₁ /amd	-0.65	True
Cd ₂ GeO ₄	Ge	Pnma	-0.24	False
K ₂ MoO ₄	K	C2/m	0.31	True
K ₂ MoO ₄	Mo	C2/m	-0.5	False
KZn ₄ (SbO ₄) ₃	Zn	R $\bar{3}$	0.44	True
Mg ₂ SiO ₄	Si	Pnma	0.16	True
Mg ₂ SiO ₄	Si	Pnma	-0.1	True
La(SbO ₃) ₃	La	Cmcm	-0.09	False
La(SbO ₃) ₃	La	Cmcm	-0.12	False
La(SbO ₃) ₃	Sb	Cmcm	0.5	False
Rb ₃ AlO ₃	Rb	C2/m	0.24	True
BaWO ₄	W	I4 ₁ /a	0.42	True
CaNb ₂ O ₄	Ca	Pbcm	-0.1	True
CaNb ₂ O ₄	Ca	Pbcm	-0.27	True
CaNb ₂ O ₄	Ca	Pbcm	0.29	True
Cs ₂ WO ₄	Cs	C2/m	0.37	True
Cs ₂ WO ₄	W	C2/m	-2.72	True
Cs ₂ WO ₄	W	C2/m	-2.27	True
K ₂ W ₂ O ₇	K	P2 ₁ /c	0.08	True
K ₂ W ₂ O ₇	W	P2 ₁ /c	-1.75	False
Cs ₂ HgO ₂	Cs	I4/mmm	0.43	True
KNa ₂ CuO ₂	K	I4mm	0.01	True
RbNb(GeO ₃) ₃	Ge	P $\bar{6}$ c2	0.43	True
RbNb(GeO ₃) ₃	Rb	P $\bar{6}$ c2	-0.06	False
Tl ₂ SnO ₃	Sn	Pnma	0.05	False
KLi ₃ PbO ₄	Pb	P $\bar{1}$	0.02	True
SrGa ₂ B ₂ O ₇	Ga	Cmcm	-0.13	False
LiIn(WO ₄) ₂	W	C2/c	0.3	True
LiIn(WO ₄) ₂	W	C2/c	0.18	True

Table S1: Energies of all distinct metastable states relative to the lowest energy symmetry-inequivalent point vacancy (ΔE), with $\Delta E < 0.5$ eV, for all metal oxides calculated in this work. Distinct metastable states are classified as those which (i) relax to a split vacancy geometry, with no corresponding symmetry-inequivalent point vacancy spontaneously relaxing to a split vacancy, or have a difference in energy >50 meV to any corresponding symmetry-inequivalent point vacancy, and (ii) are different in energy by >25 meV to all other metastable states for that vacancy.

Formula	Cation	Space Group	Energy (eV)	Split Vacancy
BaGa ₂ B ₂ O ₇	Ga	Cmcm	-0.17	False
KTlO	K	C2/m	0.4	True
Li ₂ WO ₄	W	C2/c	-0.85	True
Ga ₄ GeO ₈	Ga	C2/m	-0.41	True
NaSc(WO ₄) ₂	W	P2/c	0.15	True
NaSc(WO ₄) ₂	W	P2/c	0.08	True
TaTl(GeO ₃) ₃	Ge	P $\bar{6}c2$	0.49	True
TaTl(GeO ₃) ₃	Ge	P $\bar{6}c2$	0.28	True
K ₂ ZrGe ₂ O ₇	Ge	C2/c	-0.1	False
K ₂ Zr(SiO ₃) ₃	K	P6 ₃ /m	0.42	True
SrMoO ₄	Mo	I4 ₁ /a	0.5	True
RbTa(GeO ₃) ₃	Ge	P $\bar{6}c2$	0.41	True
RbTa(GeO ₃) ₃	Ge	P $\bar{6}c2$	0.24	True
Ca ₃ TaGa ₃ (SiO ₇) ₂	Si	P321	0.29	False
Ca ₃ TaGa ₃ (SiO ₇) ₂	Si	P321	-0.27	False
Sr ₂ MgGe ₂ O ₇	Mg	P $\bar{4}2_1$ m	-0.12	False
LiAsO ₃	As	R $\bar{3}$	-0.12	True
Al ₂ O ₃	Al	R $\bar{3}c$	-0.58	True
In ₂ O ₃	In	R $\bar{3}c$	-0.12	True
Mn ₂ O ₃	Mn	R $\bar{3}c$	-0.07	False
Mn ₂ O ₃	Mn	R $\bar{3}c$	-0.48	True
Rh ₂ O ₃	Rh	R $\bar{3}c$	0.18	True
Y ₂ O ₃	Y	R $\bar{3}c$	-0.01	True
Ti ₂ O ₃	Ti	R $\bar{3}c$	0.45	True
V ₂ O ₃	V	R $\bar{3}c$	0.43	True
V ₂ O ₃	V	R $\bar{3}c$	-0.19	True
Sc ₂ O ₃	Sc	R $\bar{3}c$	-0.16	True
Fe ₂ O ₃	Fe	R $\bar{3}c$	-0.86	True
Al ₂ O ₃	Al	C2/c	-0.58	True
PO ₂	P	C2/c	-0.23	False
PO ₂	P	C2/c	-0.09	False
V ₂ O ₅	V	C2/c	0.22	True
V ₂ O ₃	V	C2/c	0.1	False
Sb ₂ O ₅	Sb	C2/c	0.4	True
Sb ₂ O ₅	Sb	C2/c	-2.13	True
Sb ₂ O ₅	Sb	C2/c	-0.28	True
Sb ₂ O ₅	Sb	C2/c	-1.64	False
Sb ₂ O ₅	Sb	C2/c	-1.25	True
CrO ₃	Cr	C2/c	0.36	False
CrO ₃	Cr	C2/c	0.22	False
CoO ₂	Co	C2/c	-2.62	True
CoO ₂	Co	C2/c	-0.45	True
Nb ₂ O ₅	Nb	C2/c	0.22	True
Ta ₂ O ₅	Ta	C2/c	-0.45	True
CrO	Cr	C2/c	0.26	True
CrO	Cr	C2/c	-0.76	True
CrO	Cr	C2/c	-0.43	True
Al ₂ O ₃	Al	C2/m	-0.68	True
Al ₂ O ₃	Al	C2/m	-1.31	True
Al ₂ O ₃	Al	C2/m	0.33	True
MnO ₂	Mn	C2/m	0.47	True
VO	V	C2/m	-0.19	True
VO	V	C2/m	0.21	True
Y ₂ O ₃	Y	C2/m	0.46	True
V ₂ O ₃	V	C2/m	0.13	False
V ₂ O ₃	V	C2/m	-0.14	False
V ₂ O ₃	V	C2/m	-0.7	False
V ₂ O ₃	V	C2/m	-0.43	False
V ₂ O ₃	V	C2/m	-1.01	False

Table S1: Energies of all distinct metastable states relative to the lowest energy symmetry-inequivalent point vacancy (ΔE), with $\Delta E < 0.5$ eV, for all metal oxides calculated in this work. Distinct metastable states are classified as those which (i) relax to a split vacancy geometry, with no corresponding symmetry-inequivalent point vacancy spontaneously relaxing to a split vacancy, or have a difference in energy >50 meV to any corresponding symmetry-inequivalent point vacancy, and (ii) are different in energy by >25 meV to all other metastable states for that vacancy.

Formula	Cation	Space Group	Energy (eV)	Split Vacancy
V ₂ O ₃	V	C2/m	0.5	False
V ₂ O ₃	V	C2/m	-0.23	False
Sc ₂ O ₃	Sc	C2/m	0.13	False
Sc ₂ O ₃	Sc	C2/m	0.24	True
ZrO ₂	Zr	C2/m	0.47	True
TiO ₂	Ti	C2/m	-0.04	True
VO ₂	V	C2/m	0.43	True
Ga ₂ O ₃	Ga	C2/m	-0.31	True
Ga ₂ O ₃	Ga	C2/m	0.14	True
Ga ₂ O ₃	Ga	C2/m	-0.9	True
Nb ₂ O ₃	Nb	C2/m	0.45	True
Nb ₂ O ₃	Nb	C2/m	0.49	True
Nb ₂ O ₃	Nb	C2/m	-0.18	True
Nb ₂ O ₃	Nb	C2/m	0.35	True
Nb ₂ O ₃	Nb	C2/m	0.27	True
Nb ₂ O ₃	Nb	C2/m	0.11	True
Ce ₂ O ₃	Ce	C2/m	0.22	False
TeO ₃	Te	C2/m	0.33	True
TeO ₃	Te	C2/m	-0.18	True